Photocatalytic activity of TiO$_2$–SiO$_2$ nanocomposites applied to buildings: Influence of particle size and loading

Luís Pinho, Maria J. Mosquera *

TEP-243 Nanomaterials Group, Departamento de Química-Física, Facultad de Ciencias, Campus Universitario Río San Pedro, Universidad de Cádiz, 11510 Puerto Real, Cádiz, Spain

ABSTRACT

Atmospheric pollution has an evidently adverse impact on the esthetics of urban buildings and structures. Thus, the synthesis of photocatalysts capable of removing pollutants deposited on the surface of stone and other building materials is a challenge to researchers. By a simple and low cost process we have synthesized mesoporous TiO$_2$–SiO$_2$ photocatalytic coatings that meet the requirements of outdoor application. These are new materials designed to give to the building material long-term self-cleaning and strengthening properties.

We have varied the loading and size of TiO$_2$ nanoparticles in order to investigate their effect on the photocatalytic activity. We find that the integration of larger and sharper titania particles in a silica network with a titania content of around 4% (w/v) significantly improves self-cleaning effectiveness, due to the enhanced availability of surface photoactive sites. For a higher TiO$_2$ content (10%, w/v), photocatalytic action decreases because the porous volume is drastically reduced and consequently, access to photoactive sites is more difficult.

© 2013 Elsevier B.V. All rights reserved.

1. Introduction

Atmospheric pollution has an adverse impact on structures and buildings in every city of the world. Particulate matter and other components like organic and elemental carbon, and nitrogen oxides, are deposited extensively on the surface of buildings, contributing to the formation of an ugly brownish-gray to black crust. The deposition of these compounds on building facades has serious implications, not only esthetic but also economic and ecological. Scientists face a major challenge in countering air pollution and specifically in devising ways of decomposing the organic species deposited on building surfaces, a task for which TiO$_2$ can be used as a photocatalyst in coatings applied to buildings and stone structures. The application of this photocatalyst on such surfaces should lower maintenance costs by reducing surface soiling; as a consequence, there would be less need for frequent and costly cleaning operations [1].

Titania photocatalysis is produced according to the following mechanism: photons are absorbed by TiO$_2$, which generates electron–hole pairs. In contact with water, free radicals ($^\bullet$O$_2{}^-$ and OH$^\bullet$) are generated, which are able to oxidize organic matter to water and carbon dioxide, leaving no other residue. It can thus work as a self-cleaning material on the surfaces of buildings and other materials exposed to atmospheric pollution [2].

In the case of building materials based on cement or lime (concretes, mortars, etc.), several successful attempts have been made to mix the photocatalyst with the bulk material, during the processes by which these materials are prepared for use [1,3]. From the results obtained [3] it can be concluded that the addition of titania to cement, etc., gives photocatalytic properties to the material and can even improve its mechanical properties. However, few references are found in the literature about the application of TiO$_2$ photocatalysts in building materials previously formed, produced and erected, such as natural stone structures and existing buildings, ancient and modern. In these cases the conditions of application are very restrictive: because TiO$_2$ cannot be incorporated when preparing the bulk material, it must necessarily be applied to the surface of the material as a coating of some kind. In the case of application to a major structure like a building, the requirements are even stricter because the process must be carried out *in situ* under outdoor conditions, which can make the task significantly more complex and difficult. Moreover, any operation required additional to the actual application, such as heating or solvent extraction, can greatly increase the difficulties.

Regarding application on stone, in most of the references found in the literature, TiO$_2$ particles are employed dispersed in water [4,5] or incorporated in commercial products consisting of an aqueous dispersion with TiO$_2$ and an acrylic polymer [6]. But the application of such strategies cannot ensure the long-term performance of the coating because TiO$_2$ particles deposited on the surface can easily be removed from external stonework and other facing materials [4,7,8].

* Corresponding author. Tel.: +34 956016331; fax: +34 956016471.
 E-mail address: mariajesus.mosquera@uca.es (M.J. Mosquera).

One strategy for preventing the release of the TiO$_2$ from the surface to the environment would be to immobilize the photocatalyst in, for example, a SiO$_2$ matrix [9–11]. In this context, there is a valuable information resource in the previous studies made of TiO$_2$–SiO$_2$ nanocomposites for various applications in heterogeneous catalysis [12–14].

On the other hand, another target should be to produce a mesoporous photocatalyst in order to improve the access to the active sites and, consequently, to improve the catalytic activity. This can be achieved by producing a mesostructured titania [15–17] or by incorporating TiO$_2$ within a mesoporous SiO$_2$ matrix [12].

Photoactive nanocrystalline TiO$_2$ particles can be incorporated in a mesoporous silica matrix in several ways: (1) by mixing Ti alkoxide precursors with Si alkoxide [12–14]; (2) by grafting pre-synthesized silica with Ti alkoxide [18,19]; or (3) by mixing pre-formed titania colloidal nanoparticles in a Si alkoxide sol [9]. However, difficulties arise when Ti alkoxides are employed: (1) they hydrolyze much faster than Si alkoxides [14]; (2) the TiO$_2$ loading that can be achieved is quite low; and (3) the formation of photoactive TiO$_2$ crystals through a calcination process is severely limited by the low heating temperature imposed by some substrates [9]. In the case of grafting Ti alkoxide inside the silica matrix, this requires the gradual and time-consuming addition of the alkoxides to the silica in several deposition cycles [18]. Therefore, the synthesis of TiO$_2$–SiO$_2$ nanocomposites using preformed TiO$_2$ nanoparticles represents an interesting potential alternative in many fields [20–22]. In particular, it has good potential for application in coating materials for buildings because the deposition method should involve a simple application, such as aerosol-assisted process [23] with no need for any additional treatment, such as heating or solvent extraction, when applied to the exterior of the building.

We have recently designed several syntheses of products intended to protect building materials. We have prepared a consolidant product with hydrophobic properties [24,25], a stain-resistant product [26] and we have even prepared a self-cleaning product [11]. No thermal processing is required in the synthesis processes developed in our laboratory. Thus, our products find good application on thermally sensitive substrates, are more cost-effective and, especially, meet the requirements necessary for application to exterior surfaces of buildings. Some of these products are now commercially available under the corresponding exploitation patents [27,28].

In the present case of the self-cleaning product devised, a TiO$_2$–SiO$_2$ nanocomposite coating gives photocatalytic properties to stone surfaces. This product also penetrates into the pore structure of the stone, increasing its robustness. It consists of a colloidal dispersion of pre-formed titania nanoparticles dispersed in a sol of silica oligomers, in presence of a surfactant (*n*-octylamine), which is applied to stone and other building materials by means of an aerosol-assisted process. There are four fundamental reasons for adding a surfactant (such as *n*-octylamine) to our sols: (1) to prevent cracking by coarsening the pore structure of the gel network [29]; (2) to enhance photocatalytic activity by creating a mesoporous nanocomposite [11,19–21]; (3) to improve the dispersion of TiO$_2$ nanoparticles by increasing pH [30]; and (4) to act as a basic catalyst of the sol-transition inside the pore structure of the stone [24–29].

Since the textural parameters of titania–silica nanomaterials, such as their pore architecture, surface area, pore volume, pore size and TiO$_2$/SiO$_2$ packing, play an important role in their performance as photocatalysts [19,20,23], the first objective of the work reported here is to investigate the role of the nanocomposites' structure on their effectiveness as a photocatalyst; this has been done by using in the synthesis process: (1) titania particles with a range of very different particle sizes, ranging from micrometer to nanometer

scale; (2) different loadings of these titania particles. To achieve this objective, we investigate the structure of these materials in depth using several techniques including SEM, TEM/STEM and nitrogen physisorption.

Our second objective is to understand the performance of these TiO$_2$–SiO$_2$ photocatalysts on stone. Thus, we apply the materials synthesized in our laboratory on a pure limestone employed in both modern and ancient buildings, and evaluate the performance of the products for: (1) photocatalytic properties; (2) adhesion on the stone surface; and (3) strengthening the stone substratum. In addition, we also evaluate the ability of these products to meet several other important requirements associated with protective coatings for stonework, such as hydrophobic properties and esthetic characterics (i.e. the product should not induce changes in the color or appearance of the stone).

2. Experimental

2.1. Synthesis

The following reagents were used in the synthesis process: (1) TES40 WN (Wacker Chemie AG, GmbH): according to the technical data sheet, this is an ethoxysilane (average polymerization grade of 5) providing approximately 41% of silica upon complete hydrolysis and many hydrolysable ethoxy groups; (2) *n*-octylamine (Aldrich); (3) commercial colloidal AP, P25, and P90 TiO$_2$ nanoparticles, with an average particle size of 20 μm, 21 nm and 14 nm, respectively. Technical data provided by the supplier for TiO$_2$ nanoparticles are presented in the Supplementary Information (Table 1). More information on textural parameters and crystal sizes can be found in Table 2 (Supplementary Information). Since the target of this synthesis route is the mass-production of these nanocomposites, commercial products were employed due to their availability in high quantities and usefulness for large-scale production. Syntheses were carried out as follows: TES40 was mixed with TiO$_2$ nanoparticles in the presence of *n*-octylamine under high-power ultrasonic agitation (125 W cm^{-3}) without addition of solvents. The proportion of *n*-octylamine to TES40 was 0.36% (v/v). TiO$_2$ nanoparticles were added to the starting sol in three different proportions: 1, 4 and 10% (w/v). A set of formulations was prepared for each kind of particle tested. The formulations prepared were designated: S#AP, S#P25, S#P90 where # indicates the %w/v of TiO$_2$ particles included in the material (i.e. the loading). For comparative purposes, a silica material without TiO$_2$ nanoparticles was prepared according to the same synthesis; this was designated S.

2.2. Sol–gel characterization

Immediately after the synthesis of the sols, their rheological properties were studied using a concentric cylinder viscosimeter (model DV-II+ with UL/Y adapter) from Brookfield. Experiments were performed at a constant temperature of 25 °C maintained by recirculated water from a thermostatic bath. A shear stress vs. shear rate flow curve was generated. In addition, a shear stress vs. viscosity graph was also plotted. For comparison, the rheological properties of TES 40 were also evaluated.

Next, coatings of the materials under study were obtained by deposition of 3 ml of sol on plastic Petri dishes with a diameter of 85 mm. Dishes were covered and maintained at laboratory conditions (relative humidity of 60% and temperature of 20 °C). Gel transition and spontaneous drying took place. The xerogels obtained were characterized after reaching constant weight.

Powdered coatings were used for X-ray diffraction (XRD), measured on a Bruker D8 advance diffractometer equipped with a secondary monochromator, Cu tube X-ray, using Cu K$_\alpha$ radiation.

The photocatalyst coatings were visualized by scanning electron microscopy (SEM) using a FEI Sirion instrument with a field emission filament operating at 5 kV. This instrument has a resolution of 1.5 nm and it is equipped with a Through-Lens Detector (TLD) working in ultra-high resolution (UHR) mode.

The pore volume, pore size distribution and BET surface area of the materials under study were characterized by nitrogen physisorption (Autosorb IQ, from Quantachrome).

Transmission electron microscopy studies were performed in a JEOL 2010F TEM/STEM microscope, operating at 200 kV with 0.19 nm spatial resolution. This instrument is equipped with a JEOL high angle annular dark field (HAADF) detector, enabling the acquisition of STEM images. Samples were prepared by depositing a small amount of the powders directly onto Lacey-Carbon coated Cu grids. Both TEM and HAADF images were obtained.

The chemical bonds in the coatings under study were analyzed by Fourier transform infrared spectrophotometry (FTIR). The spectra were recorded in powder using a FTIR-8400S from Shimadzu ($4 \, cm^{-1}$ resolution) in the region from 4000 to $650 \, cm^{-1}$. Experiments were carried out in attenuated total reflection (ATR) mode.

Diffusive reflectance UV–vis spectra of the photocatalysts were recorded on a StellarNet Concave Grating spectrometer with an integrating sphere attachment using $BaSO_4$ powder as white reference.

Single-pulse (SP) MAS-NMR experiments were carried out on a Bruker ADVANCE WB400 spectrometer equipped with a multinuclear probe. Samples of powdered materials were packed in 4 mm zirconia rotors and spun at 8 kHz. ^{29}Si MAS NMR spectra were acquired at a frequency of 79.49 MHz, using a pulse width of 1.8 μs ($\pi/2$ pulse length = 5.4 μs), a delay time of 60 s and scan number of 2000. The chemical shift values are reported in ppm from tetramethylsilane.

2.3. Application on stone and characterization

The stone selected for evaluating the effectiveness of the materials under study is a fossiliferous limestone with a homogeneous structure composed of a micritic matrix, containing recrystallized calcium carbonate grains, and skeletal fragments of mollusks, echinoderms and foraminifera. Semi-quantitative analysis by X-ray powder diffraction analysis enabled the mineralogical composition of stone to be identified; it is composed of calcite (98.5%) and α-quartz (1.5%). This stone was selected for its whiteness, so the stains applied on its surface and the self-cleaning effectiveness of the coatings under study could be checked more easily. For all the experiments carried out, the stone samples were cut in the form of 5 cm × 5 cm × 2 cm slabs. The sols under study were applied by spraying onto the surfaces of the samples until apparent refusal, this being understood to occur when the surfaces remained wet for 1 min. After the application, the excess of sol was removed from the surface of the sample by air spraying, in order to form the thinnest possible surface film [31]. The stone samples were then dried under laboratory conditions until reaching constant weight. Uptake of products and their corresponding dry matter were calculated. The samples corresponding to untreated stone and their treated counterparts were characterized by the procedures described below, after constant weight was reached. All the results reported correspond to average values obtained from three stone samples.

Surface fragments of treated stone specimens and their untreated counterpart were examined by scanning electron microscopy (SEM) using the previously-cited FEI Sirion microscope, adopting the same conditions for observation. Cross-sections of the treated stones were observed in a JEOL 6460 LV SEM equipped with an Oxford INCAx-sight 7573 X-ray energy dispersive spectroscopy (X-EDS) detector. X-EDS elemental distribution mappings, BSE and

SE images were recorded in order to elucidate the variations in surface composition and morphology for each treatment.

The adherence of the coating to the stone surface was evaluated by performing a peeling test using Scotch® Magic™ tape (3M). The test was carried out according to previously reported methods [32].

The improvement in mechanical properties in treated stone was evaluated using the drilling resistance measuring system (DRMS), by SINT Technology. Drill bits of 4.8 mm diameter were employed with a rotation speed of 200 rpm and penetration rate of 10 mm/min.

In order to investigate the hydrophobic behavior of the coatings under study, contact angles of the stone surfaces were measured using a commercial video-based, software-controlled contact angle analyzer, model OCA 15plus, from Dataphysics Instruments.

Changes in water absorption after treatments were evaluated by applying a test of water absorption by capillarity, as recommended in UNE-EN 1925 [33]. Total water uptake (TWU) values obtained after 48 h were determined.

We also evaluated the possible disadvantage of these materials associated with changes in stone color induced by the treatments. This effect was determined using a solid reflection spectrophotometer, Colorflex model, from Hunterlab. The conditions used were: illuminant C and observer 10°. CIE La*b* color space was used and variations in color were evaluated using the parameter: total color difference (ΔE^*) [34].

The effectiveness of the materials under study as self-cleaning coatings for stone surfaces was evaluated by using a test adapted from the literature [35]. First, 1 ml of a solution of 1 mM methylene blue (Panreac) in ethanol was deposited on treated stone specimens and their untreated counterparts. Next, stone samples were irradiated with UV light working at 365 nm in a Vilber Lourmat CN15.CL chamber with 2 tubes of 15 W. The distance between the samples and the tubes was approximately 20 cm. Color variations, recorded as a function of irradiation time, were determined using the same procedure described above. The parameter: total color difference (ΔE^*) was again evaluated [34].

3. Results and discussion

3.1. Sol–gel characterization

Our photocatalysts are prepared in a one-step synthesis and applied as aerosols at ambient temperature on porous substrates. Therefore, the rheological properties of the liquids applied on stone are a key factor for surface and in-depth distribution of the photocatalysts. Sols with lower viscosity should be able to penetrate deeper into the stone, which, a priori, could be desirable. Further, a low viscosity makes the use of an aerosol generator easier for applying the product in situ [36]. In order to test viscosity, a rheological study of the synthesized sols was carried out. These viscosity data were obtained immediately after ultrasonic stirring of the dispersions. Table 1 presents the viscosity values obtained for the sols under study. For comparison purposes, the viscosity of the silica precursor employed in the syntheses (TES 40) was also evaluated. Since the behavior shown by the prepared sols was always nearly

Table 1
Viscosity for the sols under study.

Products	Viscosity (mPa s)		
	AP	P25	P90
TES40		4.82	
S		5.09	
S1	5.99	6.23	6.41
S4	11.1	11.65	10.49
S10	28.08	44.56	–

Newtonian at the shear range evaluated, viscosity was calculated as the slope of the shear rate vs. shear stress curves. In the most of the cases, the linear regression coefficients were 0.99, with the linear fit being slightly more difficult for the highest TiO_2 loading. Fig. 1 in the Supplementary Information presents the variation of the viscosity with shear stress for the sols evaluated. S10P90 has not been included in the representation because the values obtained were outside the measurement range.

The viscosity values obtained for the S sol and for the sols corresponding to the S#1 series (with the lowest TiO_2 proportion, 1% (w/v)) were very similar to those corresponding to commercial sols employed on stones and other building materials. Specifically, we determined the viscosity for one of the most popular commercial stone consolidants, Tegovakon V100 from Evonik; the viscosity of this solvent-free product was 5.25 mPa s at 25 °C [37]. Thus, we conclude that the sols prepared in our laboratory must penetrate into the stone in a way similar to that of the commercial sols, assuring adequate penetration into the stone pore structure. This is confirmed by the results obtained in the penetration evaluation test carried out as described in a later paragraph of this discussion.

Comparing the viscosity values of TES40 and S sols, these values increased slightly when n-octylamine was added to TES40. This can easily be explained by the very rapid effect of n-octylamine as a sol–gel catalyst. In the case of the TiO_2–SiO_2 sols under study, TiO_2 nanoparticles promoted a significant increase in viscosity higher than the one induced by n-octylamine. Two main trends can be observed.
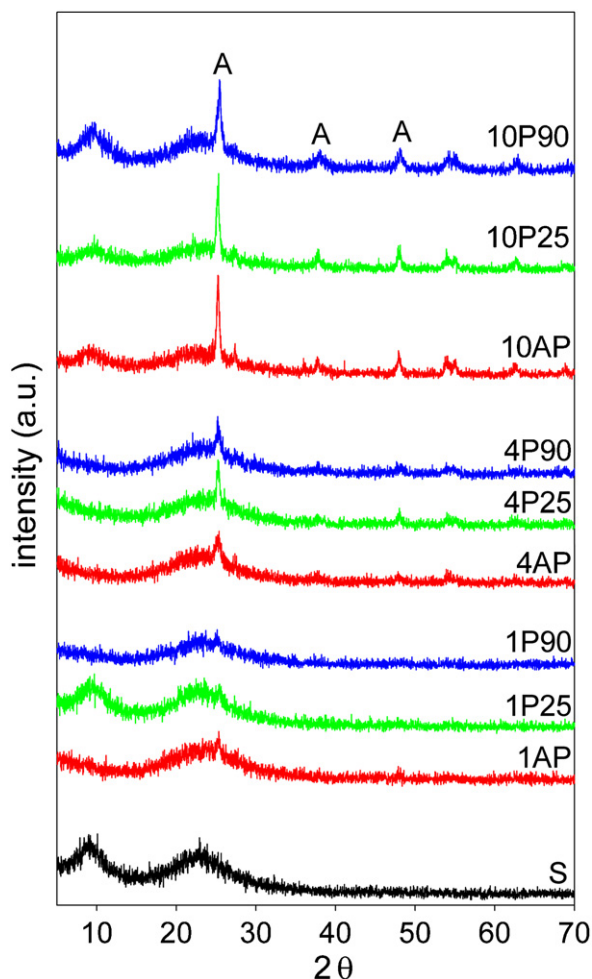
Firstly, as expected, increase of particle loading increases viscosity values. However, loading of 1% does not modify the rheological behavior of the S sol, as it has been previously reported for similar sols and loadings up to 2% (w/v) [11,37]. In the case of higher loading rates, we explain the increase in viscosity values in terms of the increase in TiO_2 particle concentration in the dispersions under study, which produces more viscous dispersions. A similar behavior was previously reported by other authors [36,38]. In addition, we also observe a progressive evolution of our sols from Newtonian to a shear-thinning behavior with the increase of TiO_2 nanoparticles concentration (Fig. S1). A similar behavior has been observed in previous studies [38,39].

Secondly, for the same TiO_2 loading, we observe a clear trend in which the increase in particle size seems to produce lower viscosity. This is, a priori, a contradictory feature because AP particles with a size in the micrometric range should promote a significantly higher viscosity than those corresponding to particles with nanometer size scales (P25 and P90). In order to understand better their behavior, we observed AP, P25 and P90 nanoparticles by SEM, before and after ultrasonic stirring in water (particle concentration 1% (w/v)), under the same stirring conditions employed in the syntheses (Fig. 2, Supplementary information). As is clearly observed by microscopy, the average size of AP nanoparticles, after ultrasonic stirring in water, is significantly reduced from a micrometer to a nanometer scale, and is close to the size presented by P25 and P90 particles. We conclude that the average AP particle size is reduced due to the strong cavitation power of ultrasonic stirring.

Regarding the trend toward increased viscosity as TiO_2 particle size is reduced, this could be attributable to the agglomeration of TiO_2 nanoparticles. This agglomeration phenomenon has previously been reported for aqueous dispersions [38]. We speculate that the aggregation of TiO_2 nanoparticles is more significant for the lowest average particle size tested (P90) as a consequence of their higher surface energy [40]. It is obvious that the aggregation takes place in order to reduce this high energy. This is a key question which will be discussed further later in this paper.

Sol–gel transition of all the sols deposited on plastic Petri dishes took place overnight, producing homogeneous composite gels. Our view is that the particles exhibit stability during the sol–gel transition because of an increase in pH values of the sol, produced by n-octylamine. In basic media, titania particles are negatively charged in the sol, because the pH is higher than the isoelectric point (IEP) of titania [30]. The IEP of P25 nanoparticles has been reported to be around 7 in water [41]. As previously discussed [39,41,42], the interaction between charged particles is based on an algebraic sum of the attractive van der Waals and the repulsive double layer forces. Near the IEP significant agglomeration takes place; large flocks with high hydrodynamic size are observed as the particle surface charge gets close to zero and attractive van der Waals forces dominate. When the pH is different from the IEP of TiO_2, surface charge is different from zero and the hydrodynamic size of the aggregates becomes smaller. We suppose that the IEP in the sols prepared in our laboratory, prior to n-octylamine addition, must be fairly close to this value. Therefore, adjusting the pH to a higher value by addition of a base (n-octylamine) to the sol must increase electrostatic repulsions and, subsequently, the stability of TiO_2 nanoparticles must be enhanced. In a similar way, electrostatic stabilization of P25 particles in polar organic solvents has previously been obtained by Kosmulski et al. [42] by adding a base such as triethylamine. Other amines or amine-terminated surfactants are also reported to stabilize TiO_2 dispersions [30,43]. It should also be noted that n-octylamine plays an important role, acting as a basic catalyst during sol–gel transition. Thus, sol–gel transition took place overnight for the three series of sols tested. This catalytic effect is a key parameter for assuring a stable dispersion of sol containing TiO_2 particles.

Fig. 1. X-ray patterns for the photocatalysts under study.

The X-ray patterns of the coatings under study are given in Fig. 1. AP, P90 and P25 TiO₂ nanoparticles, were also characterized for comparative purposes (see Fig. 3 in Supporting information). Diffractograms of all three types of nanoparticles present typical anatase and rutile peaks. All the materials prepared in our laboratory show a typical amorphous silica pattern at about 23° [44]. This confirms that our synthesis strategy does not promote an ordered pore structure, which is typical of most materials synthesized via a surfactant template. As previously reported [45], the TiO₂–SiO₂ films require a calcination process in order to produce an ordered mesostructure. Thus, we assume that our drying at ambient temperature cannot produce an ordered silica structure. In addition, we have previously obtained similar patterns for amorphous silica without any detectable order structure in gels synthesized from TEOS and *n*-octylamine [46]. We also observe that the X-ray patterns obtained show peaks previously reported to be related to pure anatase structure [44,47,48]. Specifically, the peaks assigned to anatase at around 25°, 38° and 48° were observed [47], and these are evidently more intense as the TiO₂ loading is increased. This verifies that the TiO₂ nanoparticles in the coatings prepared in our laboratory exist as separate crystalline domains, embedded within the amorphous silica matrix [22,49].

Fig. 2 shows SEM micrographs of the S material and the corresponding counterparts with TiO₂ nanoparticles, deposited on Petri dishes. All the materials form a homogeneous and continuous gel coating composed of aggregates visible at the magnification employed. Some differences can be observed with respect to the size of the aggregates comprising the gel network of the different nanocomposites under study. The S material consisted of a configuration of silica nanoparticles of nearly uniform pore size. We previously obtained a similar structure for synthesized silica materials obtained in the presence of *n*-octylamine [29] and for TiO₂–SiO₂ nanocomposites [11,37,49]. Silica nanomaterials with similar structures have been obtained by other authors in the presence of formamide [50], ammonia [51], and *n*-octylamine [52]. In this context, Bogush and Zukoski [51] developed an aggregative growth model to explain the formation of these uniform silica nanoparticles in a basic medium, such as ammonia, in which the rate of condensation is faster than the hydrolysis. In our materials, we also speculate that the formation of silica nanoparticles occurs by a similar aggregation mechanism [25,29]. We think that *n*-octylamine acts as a basic catalyst, promoting the condensation of silica oligomers present in the starting sol.

Comparatively, S forms a particulate material with a smaller and more homogeneous particle size (around 90 nm) than those corresponding to any material including titania. When TiO₂ nanoparticles (Fig. 2) are added to the sols, aggregates composed of particles are also formed. In both cases, the aggregation of smaller silica nanoparticles can be observed, thus confirming the mechanism of growth proposed. Regarding the size of the aggregates, the composites present a larger average size due to the presence of TiO₂ nanoparticles mixed with those of SiO₂, and show sizes ranging from 110 to 400 nm. In addition, in these composites, smaller particles (ranging from 20 to 50 nm) are observed on the surface of the aggregates, which we attribute to the presence of TiO₂ nanoparticles. These particles are not visible in S aggregates (Fig. 2a). Kontos et al. [53] also observed by SEM the formation of TiO₂ particles for hydrothermally treated pure TiO₂ films; these authors also attributed this finding to an aggregation phenomenon.

Regarding the effect of TiO₂ loading on the aggregate size, higher loadings cause a clear increase in the average particle size of the aggregates. This can be explained as a consequence of the larger size of the pre-formed TiO₂ nanoparticles employed in this study in comparison to the silica particles created during sol–gel transition, as postulated later when the TEM images are discussed. In addition, possible interactions produced between titania and *n*-octylamine,

Table 2
Textural parameters obtained from the isotherms and by the BJH method for the TiO₂–SiO₂ photocatalysts under study. The data presented in simple form, square brackets and in parenthesis, correspond to AP, P25 and P90 photocatalysts, respectively.

Product series	S_{total} (m²/g)	V_{pore} (cm³/g)	Pore size (nm)
S	231	0.39	6.3
S1	124 [180] (130)	0.22 [0.69] (0.29)	6.9 [13.4] (8.8)
S4	396 [90] (301)	0.49 [0.29] (0.45)	4.9 [11.7] (6.0)
S10	8.2 [90] (35.3)	0.07 [0.31] (0.07)	– [13.8] (–)

previously reported [30,54], may also play a role in the formation of aggregates. If some of the surfactant is adsorbed on the surface of the titania particles, less *n*-octylamine is available to catalyze the sol–gel transition when titania loading is raised. This could subsequently promote a suppressive effect of the silica condensation according to the proposed aggregation mechanism. This possibility is confirmed by the composites' appearance, which is more rigid for the materials without titania (S) and those with the lowest content (S1 series), which could be associated with a higher degree of silica condensation in these materials. Consequently, a gradual increase in titania loading results in the creation of smaller silica particles during the sol–gel transition. As previously indicated, these smaller particles are easily aggregated to the preformed titania particles due to their higher surface energy [40]. This produces a larger number of silica particles to be aggregated, thus creating larger aggregates in the nanocomposites with the highest titania loading (10%, see Fig. 2). This assumption is particularly evident for S10P90 where very large aggregates are formed. This could be due to the greater adsorption of *n*-octylamine caused by the large surface area of P90 TiO₂ nanoparticles.

Regarding the possible effect of the size of the titania particles, we do not observe a clear effect on the aggregate size. In the specific case of the highest titania loading, a larger aggregate size is clearly visible for S10P90 (see Fig. 2). We again associated this increase with the higher degree of aggregation occurring between the titania particles with the lowest size (P90) and the large surface area of this particles previously commented. All of these results seem to suggest that there is a critical titania particle size for promoting aggregation, which could be estimated at between 21 nm (P25 average size) and 14 nm (P90 average size).

Further, these micrographs also confirm that the initial 20 μm size of AP nanoparticles is reduced from a micrometer to a nanometer scale, close to the size presented by P25 and P90 particles, due to the strong cavitation power of ultrasonic stirring, as previously discussed.

In order to investigate in more depth the porous structure of these materials and, especially, the distribution of silica and titania particles within the aggregates, nitrogen physisorption tests were carried out. Adsorption–desorption isotherms and BJH pore size distributions obtained from the isotherm desorption branches for the materials under study are also shown in Fig. 3. The textural data obtained are given in Table 2. AP, P90 and P25 TiO₂ nanoparticles, were also characterized for comparative purposes (see Fig. 4 and Table 2 as Supporting information). All of the commercial types of preformed titania particles present a type IV isotherm with a H1 hysteresis loop, as expected for an agglomerate of TiO₂ nanoparticles [55]. Textural information on AP and P25 nanoparticles is in good agreement with the differences in their particle size. AP nanoparticles present a lower surface area but higher pore volume and pore size, which should be due to its larger particle size. In the case of P90 nanoparticles, we expected them to show values similar to P25. However, for P90 the pore size is twice as large as that corresponding to P25. We assume that this difference is due to the phenomenon of aggregation among the smallest TiO₂ nanoparticles studied. This seems to confirm again that there
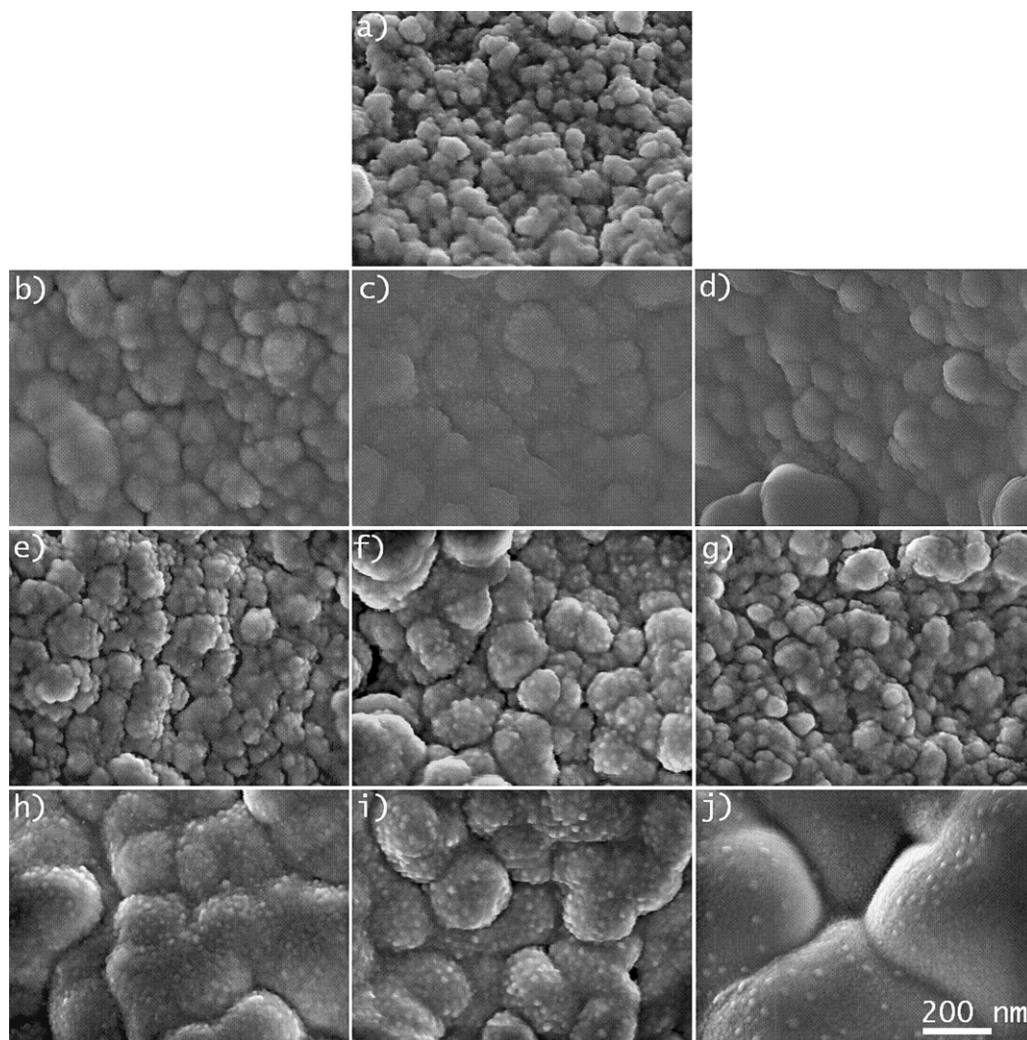
Fig. 2. SEM images of the photocatalysts under study: (a) S, (b) S1AP, (c) S1P25, (d) S1P90, (e) S4AP, (f) S4P25, (g) S4P90, (h) S10AP, (i) S10P25 and (j) S10P90.

is a critical size of titania nanoparticles, for their aggregation, of between 14 and 21 nm.

Considering the nanocomposites synthesized in our laboratory, all the materials, including S (without titania) show type IV isotherms as a consequence of the coarsening effect on the gel network exerted by n-octylamine [11]. Regarding hysteresis, most of the materials present a triangular hysteresis loop, classified as an H2 loop. In the case of the nanocomposites containing P25 particles, a type H1 hysteresis loop, characterized by parallel and nearly vertical branches, is observed. According to the literature [55], an H1 hysteresis loop is reported for materials that consist of spherical particles. In general, this loop is characteristic of materials with high uniformity of pore size and high connectivity between pores. Materials with H2 hysteresis present a similar structure but with lower connectivity. These isotherm profiles therefore suggest that all our materials are composed of a network of silica spheres, and the titania particles are integrated within this network. We have previously obtained similar morphologies [11], consisting of a dispersion of TiO_2 nanoparticles inside a regular matrix of uniform silica spheres. These results also confirm the aggregation mechanism previously proposed.

Some significant differences between these materials are observed in the titania loading effect on their texture. For titania loading rates of 1% and 4%, the SAP and SP90 materials show a pore size and pore volume similar to those obtained for the material without titania (S), while the values obtained for S1P25 are slightly higher. For the highest titania loading rate (10%), a significant reduction in pore volume is observed for SAP and S90. Other authors have found similar decreases in pore volume for increasing TiO_2 loadings [18,19]. This inverse relationship can be explained as a consequence of a higher proportion of non-porous TiO_2 nanoparticles being incorporated in the gel network.

In respect of pore size distribution, for all the titania loadings evaluated all the photocatalysts containing P25 present a more heterogeneous pore distribution at higher pore sizes. One possible explanation is that the P25 nanoparticles are more dispersed in the silica matrix. We think that AP and P90 particles, due to their larger size and greater aggregation, respectively, promote the creation of larger pore spaces inside the gel network. The size of these pores was measured by N_2 physisorption (see Table 2 in the Supplementary information), and for both of them it was around 40 nm. We speculate that these spaces are easily occupied by the silica particles created during the sol–gel transition. In the case of P25, pores are smaller (around 20 nm, see Table 2 in the Supplementary information) and they thus cannot be occupied by the silica particles. The good dispersion of the P25 particles is supported by the constant values of volume pore and pore size practically at all concentrations (see Table 2). Thus, a lower silica–titania packing that promotes a large pore size and a more heterogeneous distribution should be produced for materials containing P25. A similar
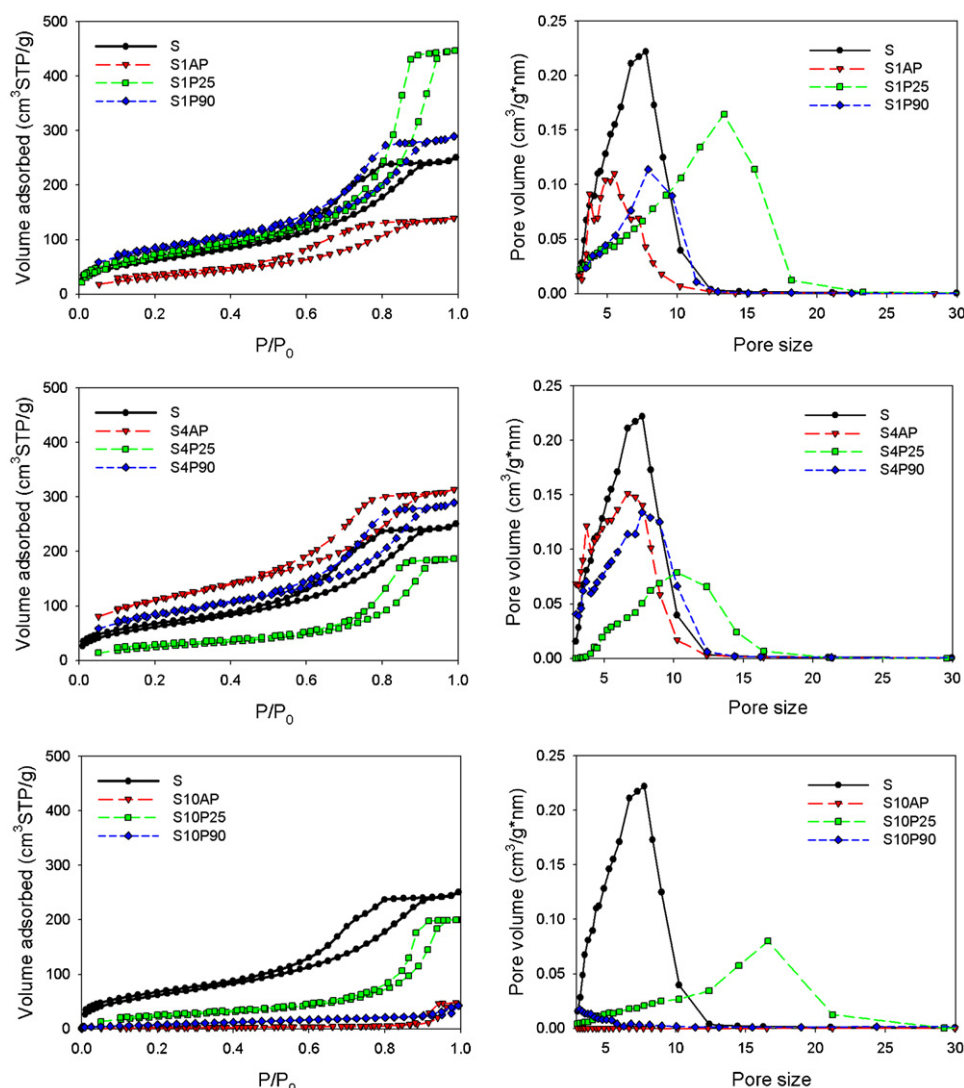
Fig. 3. Isotherms and BJH pore size distributions for the photocatalysts under study.

trend was observed for TiO_2–SiO_2 nanocomposites previously synthesized in our laboratory from P25 titania particles and the same silica precursor employed in this study [11] for loadings ranging from 0% to 2%. Fattakhova-Rohlfing et al. [21] reported that the presence of TiO_2 nanoparticles could act to open the continuous siliceous framework. Similarly, Zeleňak et al. [54] reported that interparticle space is created between the titania nanoparticles integrated within a silica matrix. Lastly, it is notable that the photocatalysts containing P90 and AP particles show significantly higher surface areas than those corresponding to P25 materials for loadings of 1% and 4%, because most of the porosity is constituted by pores of smaller size.

For a deeper investigation of the silica–titania distribution in these materials, we carried out a transmission electron microscopy (TEM) study. Fig. 4 shows representative images of S4AP, S4P25 and S4P90, acquired in TEM (a–c) and HAADF-STEM (d–f) modes. These photocatalysts were selected for this study to describe their structure in greater detail on the basis of their intermediate TiO_2-loading. In addition, they are of special interest because, as will be discussed later, these three composites showed the most efficient photocatalytic behavior. In Fig. 4a–c, individual TiO_2 nanoparticles can be observed perfectly clearly as inclusions in a SiO_2 mesoporous matrix.

These images illustrate three important features of our nanocomposites: (1) the existence of two clearly distinct and separate domains corresponding to TiO_2 and SiO_2; (2) TiO_2 presents a crystalline configuration due to the visible lattice spacing present in the structure of the material, whereas SiO_2 presents an amorphous configuration in the absence of this lattice spacing; and (3) variations in the size of TiO_2 nanoparticles and in their distribution, in the three photocatalysts, are clearly visible in the images. Fig. 4d–f (HAADF-STEM images providing contrast sensitive to compositional changes) show individual TiO_2 nanoparticles of different sizes (visibly brighter) inside the SiO_2 mesostructure. These images are particularly valuable for providing better insight into the SiO_2 porous network (which appears less bright in the image), and allowing us to confirm the TiO_2 and SiO_2 particle sizes obtained in TEM images. From these images, the following features can be established: P25 and P90 TiO_2 nanoparticles integrated in the SiO_2 matrices present an average particle size similar to that stated by the manufacturer for the individual particles (21 nm and 14 nm, respectively). It is significant that numerous aggregates of 30–80 nm size are clearly observed in the image of S4P90 whereas the S4P25 composite is composed basically of individual particles. In the case of AP particles, their disaggregation produced by ultrasound stirring resulted in the presence, in the S4AP material, of TiO_2
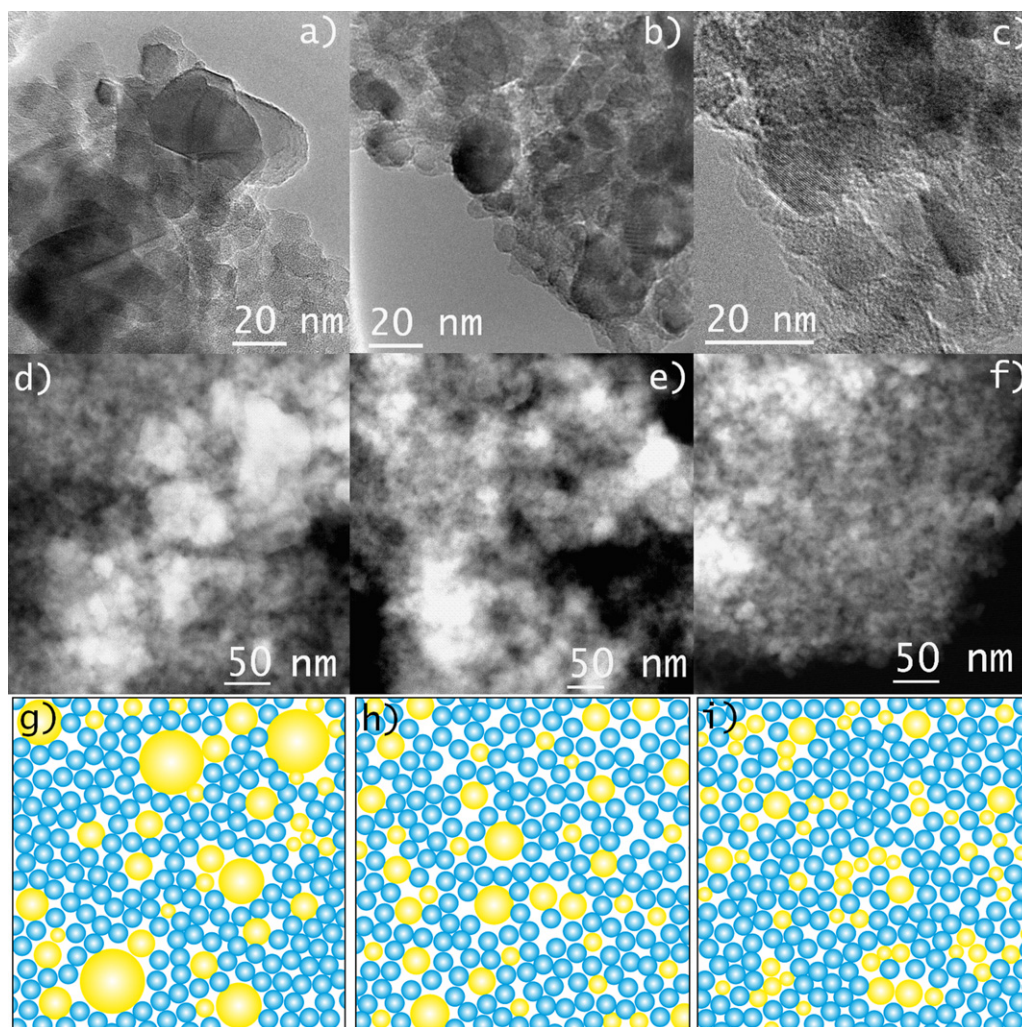
Fig. 4. Representative images of (a and d) S4AP, (b and e) S4P25 and (c and f) S4P90 obtained in TEM and HAADF-STEM modes, respectively. Schematic cross-sectional representations of (g) S4AP, (h) SP25 and (i) SP90 are also included. Ti and Si are indicated in yellow and blue, respectively. (For interpretation of the references to color in this figure legend, the reader is referred to the web version of this article.)

nanoparticles with an elongated particle shape and with a particle size of around 40–50 nm. This particle size is larger than those corresponding to S4P25 and S4P90. In addition, some smaller particles are also present.

Considering next the SiO_2 nanoparticles formed, we observe that their size is around 15–20 nm, very similar to the size of individual P25 particles. This could result in a lower degree of packing among silica and P25 titania particles than that obtained for the other preformed titania particles included in this study. In the case of AP and P90 titania particles, these produce a larger pore space (around 40 nm) into which the silica particles are more easily packed. In order to illustrate our hypothesis, a schematic model of the structures of the composites is also included in Fig. 4g–i.

FTIR spectra of the nanomaterials under study are presented in Fig. 5. All the materials, present two peaks typical of siloxanes, located at 795 and 1045 cm^{-1}, corresponding to bending and stretching vibrations, respectively [29,48]. Each spectrum also shows a peak adjacent to the stretching vibration, located at 1161 cm^{-1}. This double band (1045–1161 cm^{-1}) is associated with chains of high-molecular weight siloxanes [25,56]. This demonstrates that the sol–gel transition was effective and consequently, a high-molecular weight silica polymer has been created.

For increasing TiO_2 nanoparticles content in the photocatalysts, we observe a decrease in transmittance of between 750

and 650 cm^{-1}. Zeleňak et al. [54] attributed differences of around 620 cm^{-1} to vibrations in the TiO_2 bulk phase. After thermal treatment at 650, 850 and 1000 °C, these authors also observed a transmittance decrease in the previously cited range and attributed it to the growth of TiO_2 nanoparticles. Thus, we think that this reduction is caused by increasing the loading of TiO_2 nanoparticles integrated in the silica matrix.

The peak at 970 cm^{-1} shown in the spectra of the photocatalysts calls for particular attention. It can be attributed, *a priori*, to Si—OH stretching vibration [29]. However, the typical broad band shown for silica gels at 3250–3750 cm^{-1} associated with hydrogen-bonded silanol groups with absorbed molecular water, which should be detected together with any —OH bond, shows a weak signal in these spectra [29]. Consequently, we think that the 970 cm^{-1} peak could also be attributed to Si—N stretching vibration [57], due to hydrogen-bonded interactions that occur between the silica and the *n*-octylamine. Similarly, we [25] recently reported the presence of this Si—N interaction in the materials prepared from TES40, water and *n*-octylamine. We confirm the presence of *n*-octylamine in the photocatalysts tested in several other peaks observed in the spectra. Specifically, the bands at 1392 and 1444 cm^{-1} are attributed to *n*-octylamine C—N stretching [29,58] and C—H bending [24,58], respectively. In addition, we observe a peak at 1485 cm^{-1} which, according to the literature

Fig. 5. FTIR spectra of the photocatalysts under study.
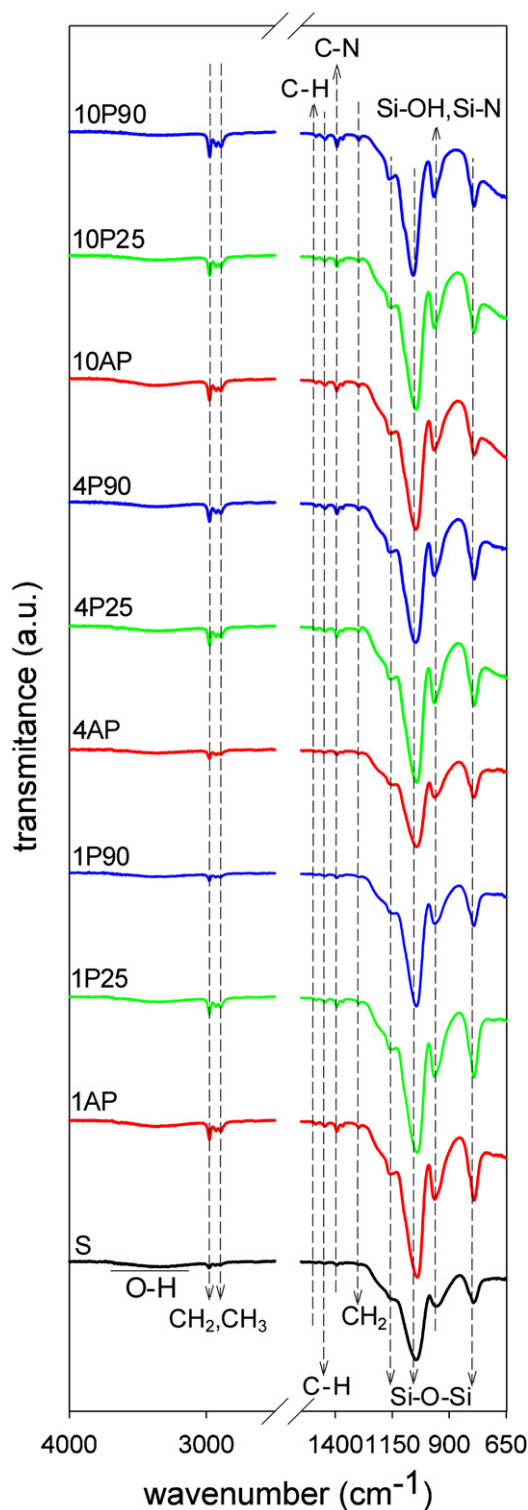

Fig. 6. UV–vis diffuse reflectance spectra of the photocatalysts under study.

[59], results from amino groups strongly hydrogen-bonded to free silanols. This confirms that the *n*-octylamine interactions with the silica precursor are produced by hydrogen bonds. The presence of *n*-octylamine in these spectra confirms that it was not completely removed during drying. In a recent paper [25], we also observe that *n*-octylamine was partially retained in silica gels dried under the same conditions.

Another contribution to the intensity of the 970 cm^{-1} peak could be that of Ti—O—Si vibrations. In previous studies, a band attributed

to these vibrations is usually observed in the 950–960 cm^{-1} zone [48]. Other authors have reported that the absorption in this zone results from both Ti—O—Si and Si—O$^-$ contributions [14]. However, the TEM images (Fig. 4) confirm that TiO$_2$ and SiO$_2$ are maintained in separate domains in our composites and consequently, an incorporation of Ti in the silica lattice has not taken place. Therefore, the interaction produced between TiO$_2$ and SiO$_2$ corresponds to van der Waals physical bonds instead of chemically bonded Ti—O—Si linkages [60].

We also observed three bands, at 2890 cm^{-1}, 2930 cm^{-1} and 2975 cm^{-1}, which we relate respectively to –CH$_3$ symmetric stretching, –CH$_2$ asymmetric stretching and –CH$_3$ asymmetric stretching [56]; these three bands are more evident in the case of S10 photocatalysts. These bands may be associated with ethoxy groups from non-hydrolyzed oligomers present in the material. Another band is observed at 1296 cm^{-1}, corresponding to CH$_2$ twist vibration, which could also be attributed to ethoxy groups [61]. A higher intensity of all these peaks is observed in the materials with higher titania content, confirming that TiO$_2$ particles exert a suppressive effect on silica hydrolysis and condensation, and consequently more non-hydrolyzed oligomers are present, as we have discussed in preceding paragraphs. In addition, the spectrum of S showed a much lower intensity for these peaks than any other of the materials.

The diffuse reflectance UV–vis spectra obtained for all the photocatalysts are shown in Fig. 6, with the object of evaluating the absorption range of the titania integrated in the silica matrix. All the photocatalysts show absorption in the UV range (up to 400 nm), and no absorption in the visible range. This means that the inclusion of TiO$_2$ nanoparticles in a silica matrix does not produce absorption in the visible range, as might be expected, for instance, in doping processes. Moreover, by comparing all our spectra with others previously obtained for TiO$_2$ P25 nanoparticles [62], we can
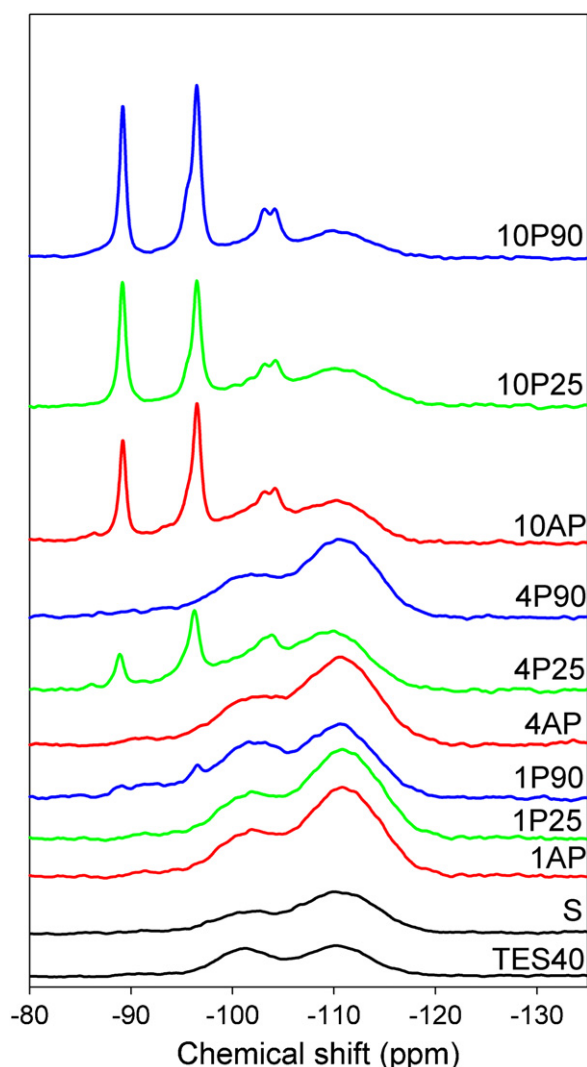
Fig. 7. ^{29}Si NMR spectra of the photocatalysts under study.

corroborate that there is no significant change of absorption after the inclusion of TiO$_2$ in a silica matrix. Similarly, Alvaro et al. [22] reported that the absorption bands were intrinsically inherent to the presence of TiO$_2$ nanoparticles and were not altered by the presence of silica domains in the solid, because Ti—O—Si bonds corresponding to a truly mixed oxide were not present in the material. This finding confirms that silica and titania are present in separate domains in the nanocomposites studied, as we previously observed by TEM (Fig. 4). Considering the location of the titania within the silica matrix, Zeleňak et al. [54] reported that titania absorption in the 350–400 nm range is related to the presence of a TiO$_2$ phase in the silica pore system or pore walls. We observed absorption in a similar range (320–400 nm), which again confirms that titania and silica are present in separate domains.

The ^{29}Si NMR spectra for all the xerogels obtained are shown in Fig. 7. All of the materials under study show two peaks at chemical shifts of −100 ppm and −110 ppm corresponding, respectively, to Q3 and Q4 structural units. In all these materials, except those with the highest titania loading (S10 series), the Q4 peak, attributable to tetrafunctional buildings, is higher than that corresponding to Q3, indicating a more cross-linked framework due to the effect of *n*-octylamine. This higher degree of reticulation is typical of silica species condensed as particles [63]. It was also observed in silica particle mesostructures obtained using amine surfactants as a

template [64]; and this was recently confirmed by us in silica materials prepared with *n*-octylamine [25]. This finding confirms that *n*-octylamine produces nanomaterials composed of a network of silica particles, as was visualized by SEM and TEM (see Figs. 2 and 4). The lower intensity observed in Q4 for S10 materials indicates, *a priori*, that less reticulation is produced.

Another significant difference according to the TiO$_2$ content was also observed. The three spectra from the photocatalysts containing the highest proportion of TiO$_2$ (S10) presented Q1 (−89 ppm) and Q2 (−91 ppm) units in conjunction with Q3 and Q4 species. Davis et al. [14] also observed an increase in signals corresponding to a reduced silica reticulation as TiO$_2$ content was raised. In our case, we speculate that this difference is due to an incomplete condensation of silica and consequently, some ethoxy groups are present in the material. This information is in good agreement with the increase of –CH$_2$– and –CH$_3$ detected through FTIR, and with the increased aggregate size detected by SEM. Here, we can confirm that these larger aggregates are also less condensed silica structures. In the case of photocatalysts with the lowest TiO$_2$ content, the signals from Q1 and Q2 are either absent or observed as a very weak signal. This finding confirms the role played by the *n*-octylamine as catalyst during the sol–gel transition, and the inhibition of its catalytic action by the presence of TiO$_2$, previously discussed in this paper.

3.2. Application on stone, and characterization

The photocatalysts synthesized in this study were sprayed as sols, under laboratory conditions, onto a building limestone in order to investigate its photocatalytic behavior, its penetration depth, adhesion to the stone, and strengthening properties. For comparison purposes, the effectiveness of S, which is only composed of silica, was also evaluated.

Uptake and dry matter of the sols under study are shown in Table 3. Although some variations were found between samples due to the heterogeneity of the limestone samples, we observe certain trends, as follows: the S sol produces the lowest uptake and dry matter among the sols applied. Uptake and dry matter percentages also seem to show a tendency to increase as TiO$_2$ nanoparticles content is raised. These trends are explained because the higher TiO$_2$ nanoparticles content means that the liquid content in the sol is lower, and thus less sol could evaporate during the sol application. Moreover, sol could also evaporate partially because carbonate stones slow down the sol–gel transition, as reported by Wheeler et al. [65].

Fig. 8 shows SEM images of stone specimens treated with the photocatalysts under study and their counterpart without titania. All of the materials under study form a crack-free, homogeneous and coarse coating on the stone surface. This confirms the contribution of *n*-octylamine in reducing the capillary pressure responsible for cracking. As we have previously stated [11,24,25,29], the surfactant reduces capillary pressure in two different ways: (1) by coarsening the gel network pore size; and (2) by reducing the surface tension of the starting sol. It should also be noted that the coarsening produced by *n*-octylamine must also improve the access to photoactive sites, thus increasing the photocatalytic activity.

We also observe some changes in the morphology of the coatings when TiO$_2$ nanoparticles are integrated in the silica network. Specifically, the higher titania loading produces larger aggregates, in good agreement with the behavior observed from the coatings produced on Petri dishes previously discussed in this paper (Fig. 2). This allows us to corroborate that the stone substrate has little influence in the final surface morphology of these photocatalysts.

We investigated the penetration depth of the sols by using SEM to visualize a cross section of the limestone samples treated. X-EDS elemental mappings for Ti and Si were also obtained. All the

Table 3
Properties of the treated stone specimens and the untreated counterparts.[a]

	% (w/v) TiO$_2$	Uptake (%, w/w)	Dry matter (%, w/w)	Material removed by peeling (mg)	Contact angle (°)	ΔE^*	TWU (%, w/w)
U[b]	–	–	–	2.3 ± 0.1	61 ± 9	–	5.58 ± 0.12
S	0	1.40 ± 0.05	0.82 ± 0.01	0.3 ± 0.1	91 ± 4	3.35 ± 0.10	0.10 ± 0.00
AP	1	1.96 ± 0.17	1.31 ± 0.23	0.2 ± 0.0	99 ± 13	3.31 ± 0.18	0.08 ± 0.04
	4	2.68 ± 0.00	1.44 ± 0.40	0.4 ± 0.2	90 ± 2	2.20 ± 0.19	0.07 ± 0.01
	10	2.26 ± 0.36	1.57 ± 0.45	1.0 ± 0.0	85 ± 4	4.51 ± 1.89	0.13 ± 0.09
P25	1	1.77 ± 0.60	1.64 ± 0.21	0.1 ± 0.1	106 ± 6	2.41 ± 0.30	0.32 ± 0.10
	4	2.97 ± 0.03	1.44 ± 0.41	0.6 ± 0.2	79 ± 3	4.60 ± 0.13	0.08 ± 0.02
	10	1.97 ± 0.01	1.26 ± 0.04	2.0 ± 0.9	85 ± 4	2.95 ± 0.05	0.06 ± 0.01
P90	1	2.00 ± 0.05	0.95 ± 0.03	0.3 ± 0.1	102 ± 6	3.66 ± 0.03	0.35 ± 0.12
	4	1.89 ± 0.03	1.23 ± 0.01	0.8 ± 0.4	90 ± 2	3.19 ± 0.20	0.09 ± 0.03
	10	2.16 ± 0.49	1.61 ± 0.39	0.7 ± 0.4	87 ± 3	3.01 ± 0.08	0.08 ± 0.01

[a] Data correspond to average values. Standard deviations are also included.
[b] Untreated stone sample.

sols show a similar behavior when they are applied on the stone. As an example, the X-EDS mappings obtained for cross-sections of limestone treated with S#AP photocatalysts are shown in Fig. 9. Mappings corresponding to limestone samples treated with S are also included for comparison purposes. These mappings allow us to confirm that S presents a deep penetration of Si across all the depth range evaluated (2.0 mm). S1AP shows that both Ti and Si penetrate to a very similar depth. In the case of the materials with
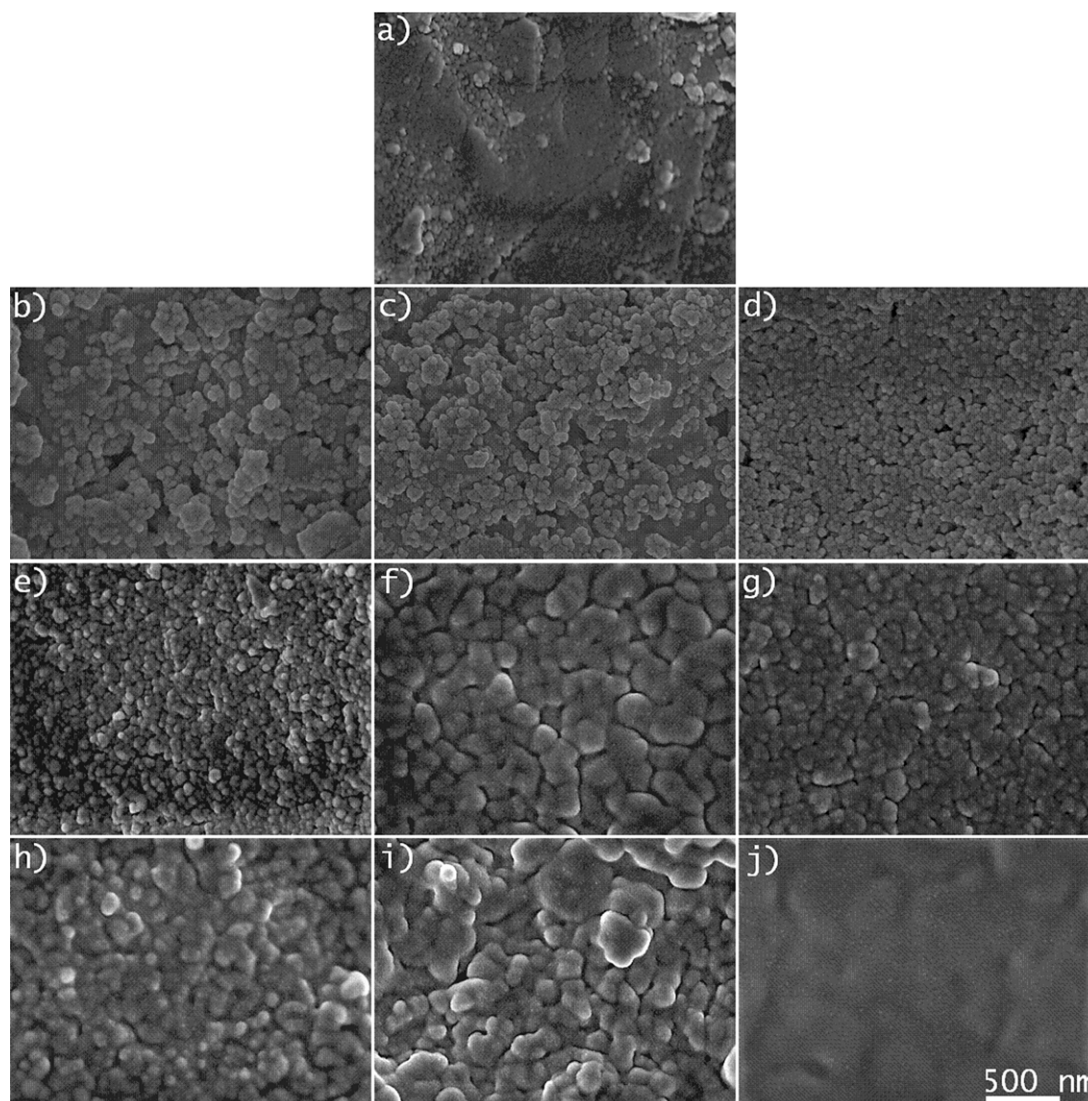

Fig. 8. SEM images of the photocatalysts under study applied on stone: (a) S, (b) S1AP, (c) S1P25, (d) S1P90, (e) S4AP, (f) S4P25, (g) S4P90, (h) S10AP, (i) S10P25 and (j) S10P90.
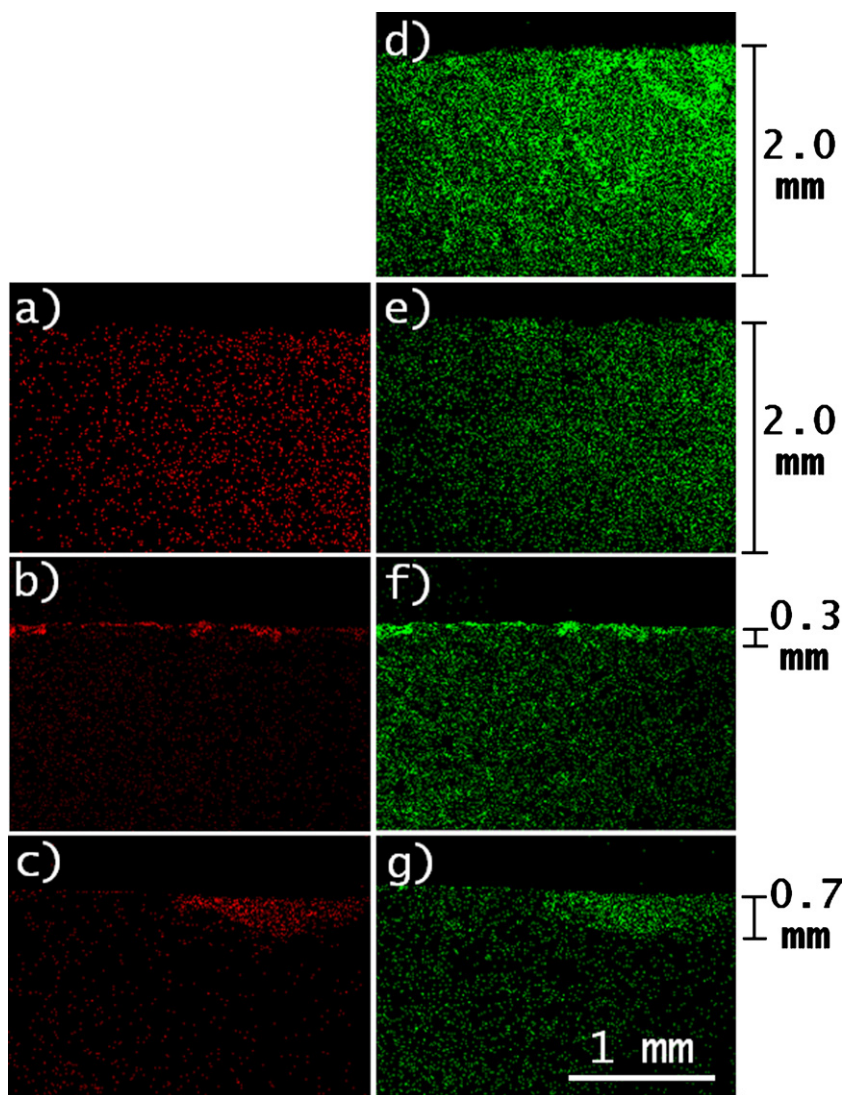
Fig. 9. X-EDS elemental mappings for Ti (red) and Si (green) present in the cross section of limestone samples treated with (d) S, (a and e) S1AP, (b and f) S4AP, and (c and g) S10AP. (For interpretation of the references to color in this figure legend, the reader is referred to the web version of this article.)

higher titania loading (S4AP and S10AP), we also observe a significant accumulation of Ti and Si, ranging between 0.3 and 0.7 mm, on the surface of the stone. This finding could be associated with the higher viscosity of these coatings with the highest contents in titania particles.

In order to confirm this conjecture, Fig. 10a presents a BSE image of the cross-section of the limestone sample treated with S4AP. Images with higher magnification were obtained on the surface (indicated in blue, Fig. 10b and c) and in the interior (indicated in yellow, Fig. 10d and e) of the stone in SE and BSE modes, respectively. From this more detailed analysis of the cross section of S4AP we can observe that a thin photoactive surface film is formed (Fig. 10b) which also penetrates between the stone grains. The presence of the photocatalyst between the grains is clearly visible in Fig. 10c because of the higher atomic number of Ca with respect to Si. We thereby corroborate that our photocatalyst is able to adhere to the limestone, a characteristic essential for its potential long-term performance [7]. We do not obtain the same result for the deeper zones of the limestone (Fig. 10d, SE mode; Fig. 10e, BSE mode), probably because the deeper zone has a lower content of S4AP, as confirmed by the results previously obtained by SEM.

Since one significant drawback of commercial products applied on stone has been the reduced photocatalytic efficiency found during long-term use, due to the elimination of TiO_2 from the stone surface [7,11], we have also investigated the degree of adhesion of the coatings applied on stone, by performing a peeling test adapted from the literature [32]. Table 3 shows the weight lost by the untreated stone and its treated counterparts after testing.

The greatest loss of mass after the peeling test is observed for the untreated stone (see Table 3). This happens because the untreated stone surface presents a considerable amount of loose matter which can easily be detached through our adhesion testing method. Stone samples treated with S and S1 photocatalysts show almost negligible loss of mass (see Table 1). These findings confirm that TiO_2 has been integrated into the silica matrix, which has, in turn, adhered firmly to the stone. In this respect, the inclusion of the photocatalyst in a mesoporous silica coating is an interesting solution for keeping particles well adhered to the surface, to provide long-term wear resistance.

For higher TiO_2 nanoparticles content the test removed a slightly larger amount of material from the stone surface, reaching a maximum for the coatings with the highest TiO_2 content (S10). We associate this result with the formation of a less condensed and more detachable composite on the limestone surface for coatings with the highest titania loadings, as was previously confirmed through ^{29}Si NMR. Specifically, the stone treated with S10P25
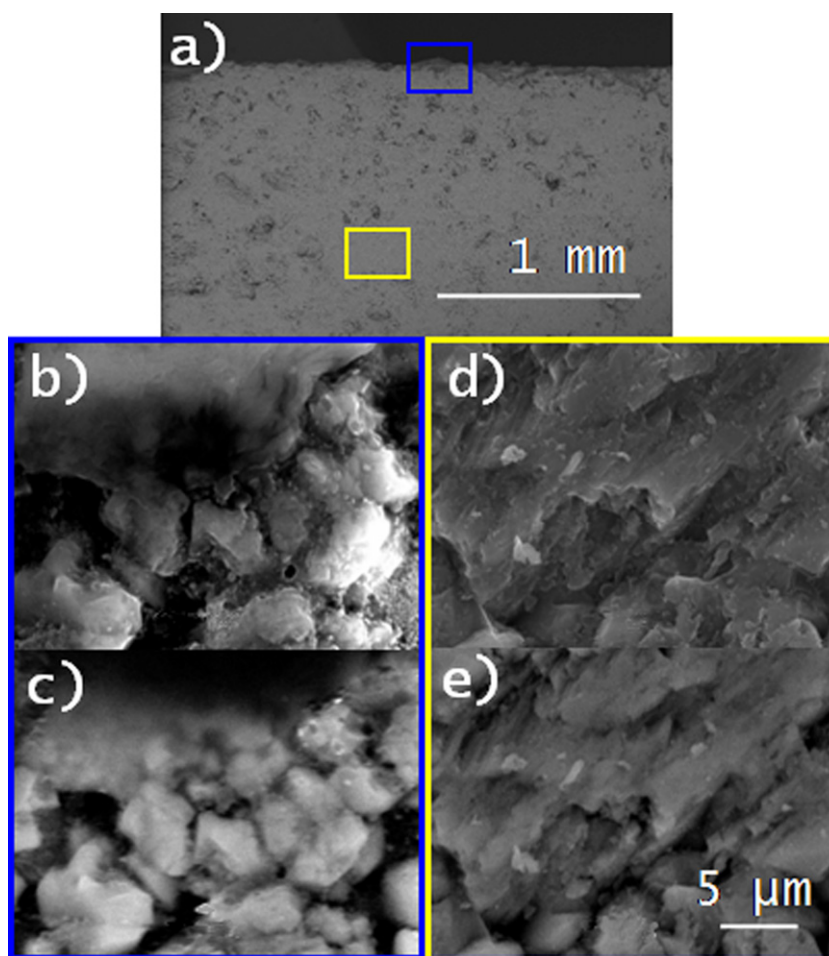
Fig. 10. Surface (b and c) and in-depth (d and e) images of the cross section of the limestone sample treated with S4AP. (b) and (d) were obtained in SE and (a), (c) and (e) in BSE imaging mode. The area analyzed in (a) corresponds to the X-EDS elemental mappings present in Fig. 9(a) and (e).

showed the highest value of material mass removed. We think that this finding could be associated with its very high porosity, which produces more air voids; this could make more material adhere to the peeling tape.

We also investigated whether any enhanced strengthening of the stone was produced by the products applied; this was done by measuring and comparing the drilling resistance of the untreated limestone and its treated counterparts. The device used has been designed specifically to evaluate mechanical resistance of stone, and provides a very high discriminating power [66]. Fig. 11 shows the profiles obtained in this study.

Some significant differences were observed in line with variation in the titania loading. The material without titania (S) produces the greatest increase in mechanical resistance; and the samples treated with the lowest titania loading composites show resistance values similar to those obtained for the stone treated with the material without TiO_2. This demonstrates that a 1% loading is not enough to modify the robustness produced by the composite formed into the stone pore structure. The materials with higher titania loading showed reduced drilling resistance. This result could be explained as a consequence of the very low degree of reticulation and condensation of the gel networks, as we have previously discussed.

Comparing the two materials with the higher titania loadings, we observe that the 4% loading produced the least reduction in stone resistance, nearly to the value obtained for the untreated stone. We attribute the increase in resistance of the composites

with the highest titania loading to the titania particles being more robust than the silica gel network.

We also consider that these test results confirm that *n*-octylamine is playing a valuable role in enhancing the robustness of the treated stone, since silicon-based products are known to be ineffective as consolidants on pure carbonate stones [31,67]. In a previous study, we found increased drilling resistance for the same limestone using a SiO_2/TiO_2 hybrid coating material obtained in the presence of *n*-octylamine [11].

Since water is the main vehicle carrying the agents of decay, such as soluble salts, microorganisms, etc., that attack building materials, any hydrophilicity in a coating would be undesirable. Therefore, we have also measured water droplet static contact angles on the surface of stone samples treated with the photocatalysts under study. Results obtained are given in Table 3. The untreated limestone samples show a low contact angle (61°) due to the hydrophilic character of the stone. We observe that static contact angles are higher for the stones treated with composites with the lower TiO_2 nanoparticles contents. Specifically, the S1 and S4 photocatalysts show a hydrophobic behavior, with a static contact angle value higher than 90° or close to this value. When more TiO_2 nanoparticles are loaded in the photocatalysts, there is a decreasing tendency in the static contact angles due to the hydrophilic character of TiO_2 nanoparticles, as we have reported before [11]. These results demonstrate that the nanocomposites with 1% and 4% titania loading do not produce water absorption and thus can be employed as hydrophobic coatings in stones and other building materials.
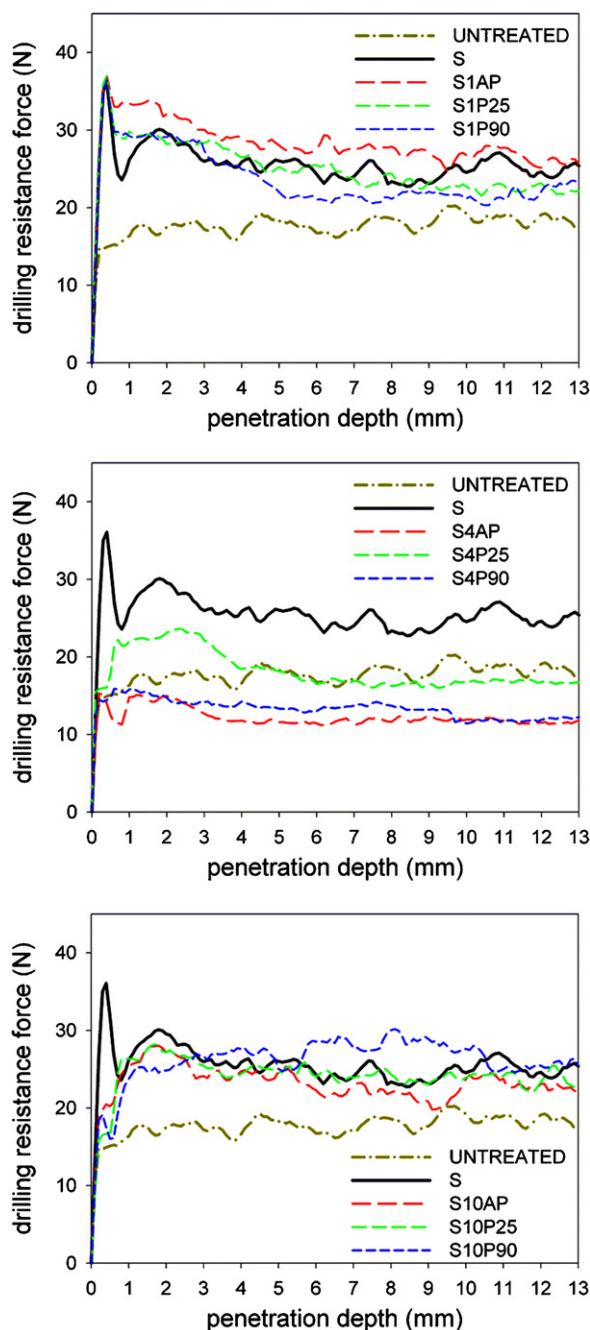
Fig. 11. Drilling resistance profiles for the limestone under study after the application of our photocatalysts.

In order to confirm the ability of the composites to prevent penetration of water into the stone, we carried out a test of water absorption by capillarity. Total water uptake (TWU) values obtained after 48 h are shown in Table 3. The results confirm the hydrophobic behavior of the composites, since the uptake values obtained are close to zero and significantly lower than that obtained for the untreated counterpart. These results demonstrate that the nanocomposites do not produce water absorption and thus can be employed as hydrophobic coatings on stones and other building materials.

Another very practical limitation on the prospective employment of these products would be encountered if they produced changes in the color of the stone treated. Therefore, total color difference values (ΔE^*) of the stone induced by the photocatalysts

were measured and these results are given in Table 3. All the photocatalysts produced color changes close to the generally accepted threshold value $\Delta E^* \leq 5$, even for the most restrictive applications such as ancient building restoration [68]. This parameter is particularly critical for materials containing TiO_2, which is widely used as a white pigment for its considerable hiding power. By dispersing particles of sizes reduced to the nanoscale, these coatings also reduce the hiding power of TiO_2 and minimize the possibilities of significant color change. In addition, we propose removing the excess of sol on the stone surface directly after its application. We confirmed that, by using this application method, it was possible to reduce the color change to suitable values for application on stone surfaces and buildings.

Finally, and most importantly, we have investigated the self-cleaning properties of the photocatalysts synthesized in our laboratory and applied to the limestone tested, by carrying out a photo-degradation test of stains deposited previously on the stone surface. Methylene blue (MB) was used as the staining agent, dissolved in ethanol in order to ensure rapid evaporation of all the liquid. The evolution of total color differences (ΔE^*) under UV light, with the time was recorded, and results are shown in Fig. 12, for the photocatalysts under study. Limestones treated with S and also untreated samples were included in this test for comparison purposes. In order to confirm the changes in color undergone by the specimens under study, Fig. 13 shows images, observed by optical microscopy, of the surface of the stone samples, obtained at the end of the photocatalytic test.

The conditions of this test make the following comments relevant: (1) It was performed in the absence of liquid water and with low relative humidity (around 30%); therefore, degradation times are necessarily slower than in experiments carried out in high moisture, because the generation of OH• free radicals is reduced; in our view, if these products are applied on buildings outdoors, the moisture present in the environment would probably accelerate the photodegradation process; (2) Our test has been carried out in the presence of atmospheric oxygen and at neutral pH conditions, thus ensuring that all the color variations are due to the elimination of MB, and not to the undesirable formation of the leuco form of MB (LMB) [69]; (3) We have evaluated photodegradation by measuring the total color variation parameter because this is usually considered for portable color measurement; this makes it very useful for testing the degradation, *in situ*, in construction, restoration or rehabilitation of buildings.

Regarding the results obtained (see Fig. 12), the final ΔE^* value reached for the untreated stone is 38.3, after more than 1000 h of exposure, corresponding to a "natural" reduction of 17%. Bleaching of methylene blue (MB) under visible/UV light has been reported previously, and this bleaching has been associated with the absorption of light undergone by the dye in the 350–520 nm range [69].

In the case of the limestone samples treated with the photocatalysts synthesized in this study, from the profiles two different rates of degradation at different times can be clearly distinguished. Very rapid MB bleaching occurs in the first 72 h. Next, a slower rate of degradation is observed over the longer term. As we reported previously [11,37], we think the photocatalytic action of the TiO_2 particles produces most of the total degradation effect on the stain in the first few hours of exposure (the first part of the curve). We speculate that the second stage, with a much slower rate of degradation, may be caused by an effect of the SiO_2/TiO_2 coating initially reducing the capacity of the MB to penetrate into the limestone pore structure. Thus, MB is retained on the stone surface where it can be degraded more easily than that located deeper in the pore structure of untreated stone. This hypothesis is corroborated by the behavior observed for the stone samples treated with the material without TiO_2 (S). Obviously, the first stage of curve associated with the photocatalytic action of the TiO_2 is not observed in
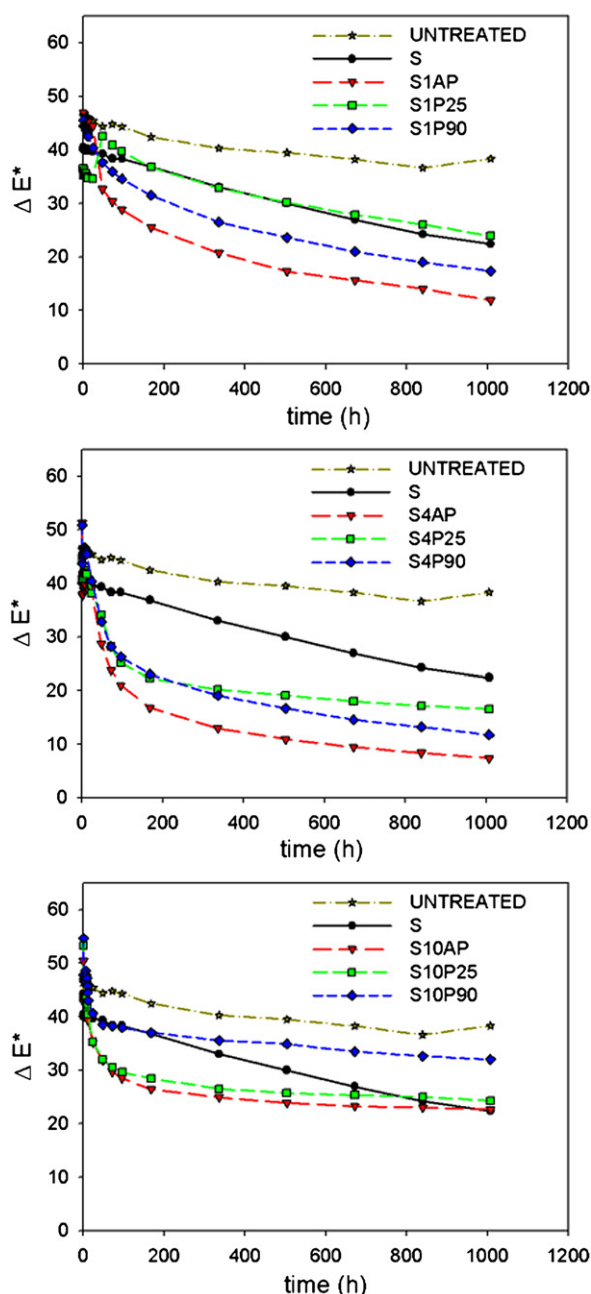
Fig. 12. Evolution of total color difference (for methylene blue stains) on treated and untreated samples of limestone. The samples were previously stained with methylene blue and then irradiated with UV light ($\lambda_{min} = 365$ nm) for more than 1000 h.

these samples. However, a degradation profile similar to that corresponding to the second stage shown in the samples coated with the nanocomposites is clearly observed. We again attribute this degradation profile to the effect of silica coating reducing MB penetration into the limestone pore structure.

Considering now the effect of the TiO$_2$ loading on the photocatalytic performance of the nanocomposites under study, we observe that increasing the TiO$_2$ content from 1% to 4% enhances the photocatalytic activity, as was expected. This is confirmed by the significantly shorter first stage of the curve (due to photocatalytic activity) in materials containing 1% titania loading. However, increasing the titania loading to 10% is clearly counterproductive. The final color observed on the stone surface of the samples confirms this conclusion (see Fig. 13). We explain this significantly

reduced photocatalytic activity in terms of the structure of these nanocomposites. The substantial reduction in pore volume and BET surface area for the materials containing the highest titania content (see Table 2 and Fig. 3) could be responsible for the reduced photocatalytic effectiveness observed. We [11] and other authors [20] have previously reported that the photocatalytic degradation of MB is clearly enhanced by the addition of TiO$_2$ particles to a SiO$_2$ mesoporous structure, in contrast with the weaker effect observed when the particles are integrated in a dense microporous matrix.

From the results discussed above, we can conclude that mesostructure of the photocatalyst, created by the *n*-octylamine, plays an important role in the photocatalytic activity of the materials under study. Thus, the nanocomposites with the highest titania loading, remarkably, show the weakest photocatalytic activity due to their very small pore size and specific surface; in fact, they hardly present any pores in the mesopore range. In contrast, the effectiveness of the other photocatalysts is enhanced because they are mesoporous materials with a larger surface area and pore volume. Other authors have obtained similar results [18,19,21,54]. This enhancement effect in photocatalytic activity was explained by Suzuki et al. [20] in terms of the increased BET surface area, which accelerates the diffusion of MB toward the reaction sites (i.e. toward the TiO$_2$ nanoparticles). In addition, we [11] have reported that the presence of mesopores also assists rapid MB diffusion. Moreover, we think a synergistic effect occurs with the SiO$_2$ matrix, which acts as an absorber and provides access to the TiO$_2$ photocatalytic sites. This hypothesis is clearly confirmed by the degradation profiles observed in the photocatalysts with highest titania loading, in which degradation profile is significantly lower because access to photoactive sites was significantly reduced.

A comparison of the three nanocomposites loaded to 4% with TiO$_2$ of different particle size also reveals certain differences. Specifically, S4AP, S4P90 and S4P25 present final ΔE^* values of 7.4, 11.8 and 16.6, respectively. The lower pore volume and pore size of S4P25 may be the explanation why it performs worse than the other two S4 photocatalysts (see Table 2), supporting the above hypothesis.

The size of the TiO$_2$ particles used has a clear effect on photocatalytic performance of these materials. We find that the S#AP photocatalysts always have a better performance than the S#P90 and S#P25 counterparts. It seems that the higher average size and the sharper shape of the TiO$_2$ nanoparticles present in S#AP, as observed by TEM/STEM, favors their photocatalytic effectiveness. The effect of particle size on TiO$_2$ photocatalysts has been reported previously by several authors [70–72], who found that larger titania particles have greater effective surface area for greater photon absorption and electron–hole generation and, thus, produce a better photocatalytic performance. Regarding the effect of particle shape, Li and Liu [73] suggested previously that sharper titania particles could be inherently more reactive in photo-oxidation. In our case, the AP particles used are sharper than the other types because the high-power ultrasonic agitation applied in the synthesis changes the particles from a regular spherical form (see Fig. 2 in the Supplementary information) to an irregular and sharper shape (see Fig. 4).

Another complementary characteristic that may enhance the photocatalytic activity in the S4AP materials is their higher BET surface area. We observe that the increasing surface area for S4 materials promotes increased photocatalytic effect (AP > P90 > P25). This trend was confirmed by Yoshida et al. [74]. This effect is not observed with the other loadings tested either because titania content is too low (S1) or because a non-porous network is created (S10). The final color observed on the stone surface confirms that the S#P25 and S#P90 photocatalysts have a weaker photocatalytic performance in comparison with the S#AP nanocomposites (Fig. 13).
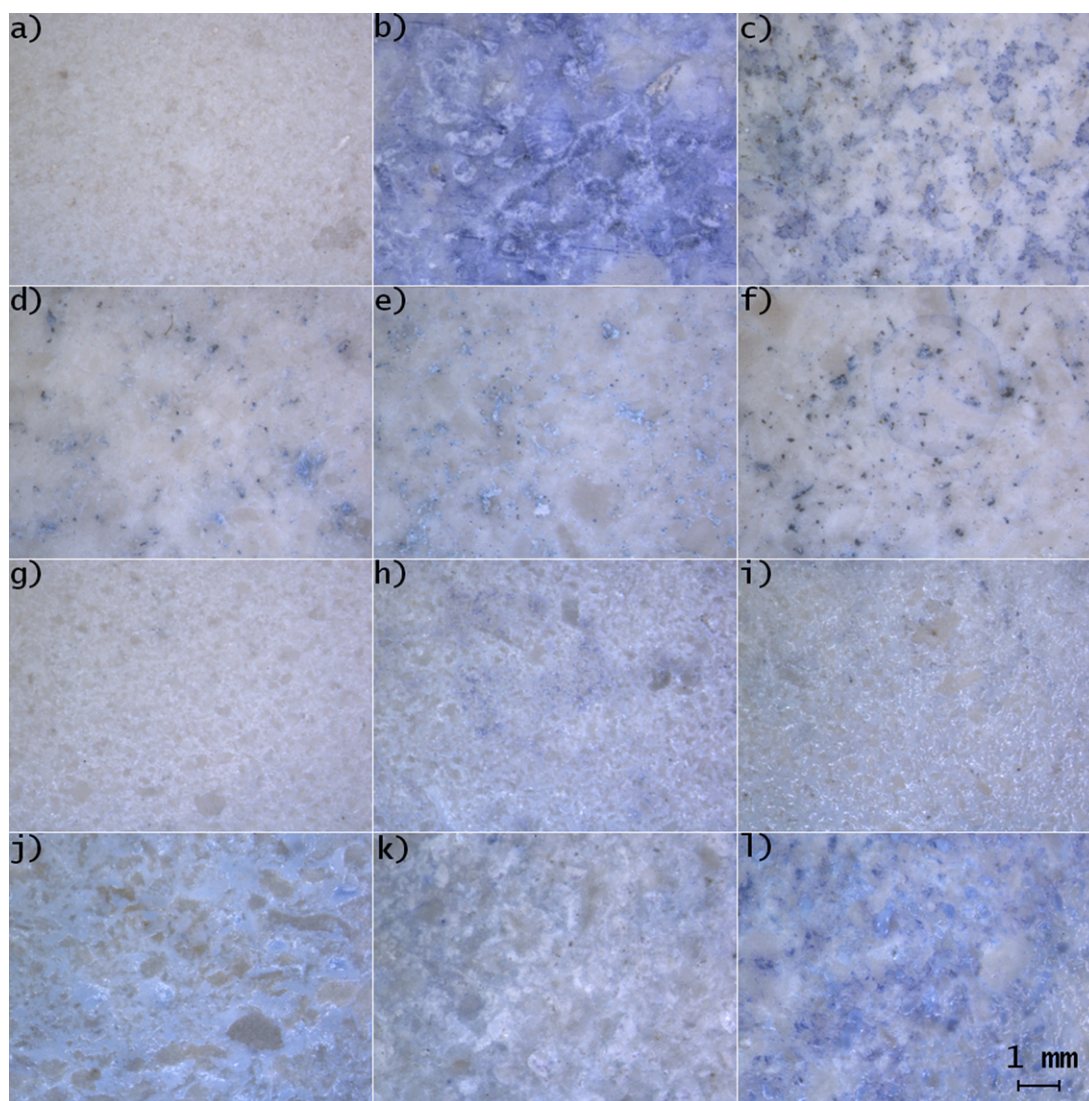
Fig. 13. Representative optical microscopy images of the final color of the stone surface obtained after the self-cleaning test consisting of more than 1000 h of UV light ($\lambda_{min} = 365$ nm) irradiation. Image (a) corresponds to the untreated stone sample before staining and is included for comparison purposes. The untreated stone sample tested corresponds to (b). The samples subjected to treatment and tested are (c) S, (d) S1AP, (e) S1P25, (f) S1P90, (g) S4AP, (h) S4P25, (i) S4P90, (j) S10AP, (k) S10P25 and (l) S10P90.

4. Conclusions

We have designed an innovative and simple synthesis route for producing TiO_2 and SiO_2 photocatalysts with application on stones and other building materials. Since the route simply consists of mixing of silica oligomer, titania particles and a surfactant, the process can easily be adapted for mass-production of the product. In this synthesis, a surfactant constituent acts: (1) to disperse the titania particles; (2) to catalyze the sol–gel transition; and (3) to coarsen the porous gel network, thus providing better access to photoactive sites. We demonstrate that these photocatalysts present self-cleaning properties on the limestone evaluated, are able to adhere firmly to the stone, and improve stone robustness.

From our in-depth investigation of the texture of these photocatalysts, we conclude that this is a key parameter for the efficacy of the photocatalytic activity. Specifically, the incorporation of larger and sharper titania particles within a silica network significantly improves the effectiveness of the photocatalyst on the stone, and subsequently enhances its self-cleaning effect. Thus, we can conclude that the size and shape of the titania particles play a crucial role in photocatalytic activity of the nanocomposites synthesized in this study. We attribute this improvement

to the high availability of photoactive surface sites in these materials.

We also demonstrate that increasing the titania loading (up to an optimal content of 4%) produces an improvement in photocatalytic activity. For a higher content (10%), this activity decreases, because the pore volume of the nanocomposite is drastically reduced and consequently, access to photoactive sites is more difficult. Moreover, a 10% loading has the following disadvantages, due to the *n*-octylamine reducing the catalytic effect during sol–gel transition: (1) weaker adherence to the stone; and (2) less strengthening imparted to the stone.

Finally, we believe that the photocatalysts synthesized have clear practical applications, because the products obtained by this route meet the user requirements for a photocatalytic coating that can be applied externally, outdoors, in a simple and low-cost process, and which preserves the esthetic qualities of the stone.

Appendix A. Supplementary data

Supplementary data associated with this article can be found, in the online version, at http://dx.doi.org/10.1016/j.apcatb.2013.01.021.

References

[1] I. Karatasios, M.S. Katsiotis, V. Likodimos, A. Kontos, G. Papavassiliou, P. Falaras, V. Kilikoglou, Applied Catalysis B 95 (2010) 78.
[2] A. Fujishima, T. Rao, D. Tryk, Journal of Photochemistry and Photobiology C 1 (2000) 1.
[3] M. Lackhoff, X. Prieto, N. Nestle, F. Dehn, R. Niessner, Applied Catalysis B 43 (2003) 205.
[4] I. Poulios, P. Spathis, A. Grigoriadou, K. Delidou, P. Tsoumparis, Journal of Environment Science and Health Part A: Environmental Science 34 (1999) 1455.
[5] E. Quagliarini, F. Bondioli, G. Goffredo, C. Cordoni, P. Munafò, Construction and Building Materials 37 (2012) 51.
[6] M.F. La Russa, S.A. Ruffolo, N. Rovella, C.M. Belfiore, A.M. Palermo, M.T. Guzzi, G.M. Crisci, Progress in Organic Coatings 74 (2012) 186.
[7] K. Rao, M. Subrahmanyam, P. Boule, Applied Catalysis B: Environmental 49 (2004) 239.
[8] L. Windler, C. Lorenz, N. von Goetz, K. Hungerbühler, M. Amberg, M. Heuberger, B. Nowack, Environmental Science and Technology 46 (2012) 8181.
[9] A. Pénard, T. Gacoin, J. Boilot, Accounts of Chemical Research 40 (2007) 895.
[10] H. Kibombo, R. Peng, S. Rasalingam, R. Koodali, Catalysis Science & Technology 2 (2012) 1737.
[11] L. Pinho, M.J. Mosquera, Journal of Physical Chemistry C 115 (2011) 22851.
[12] W. Zhang, M. Fröba, J. Wang, P. Tanev, J. Wong, T. Pinnavaia, Journal of the American Chemical Society 118 (1996) 9164.
[13] M. Kruk, M. Jaroniec, A. Sayari, Microporous Materials 9 (1997) 173.
[14] R. Davis, Z. Liu, Chemistry of Materials 9 (1997) 2311.
[15] T. Kimura, Y. Yamauchi, N. Miyamoto, Chemistry – A European Journal 17 (2011) 4005.
[16] T. Kimura, Y. Yamauchi, N. Miyamoto, Chemistry – A European Journal 16 (2010) 12069.
[17] H. Oveisi, S. Rahighi, X. Jiang, Y. Nemoto, A. Beitollahi, S. Wakatsuki, Y. Yamauchi, Chemistry – An Asian Journal 5 (2010) 1978.
[18] K. De Witte, V. Meynen, M. Mertens, O.I. Lebedev, G. Van Tendeloo, A. Sepúlveda-Escribano, F. Rodríguez-Reinoso, E.F. Vansant, P. Cool, Applied Catalysis B 84 (2008) 125.
[19] E. Beyers, E. Biermans, S. Ribbens, K. De Witte, M. Mertens, V. Meynen, S. Bals, G. Van Tendeloo, E.F. Vansant, P. Cool, Applied Catalysis B 88 (2009) 515.
[20] N. Suzuki, X. Jiang, L. Radhakrishnan, K. Takai, K. Shimasaki, Y. Huang, N. Miyamoto, Y. Yamauchi, Bulletin of the Chemical Society of Japan 84 (2011) 812.
[21] D. Fattakhova-Rohlfing, J. Szeifert, Q. Yu, V. Kalousek, R. Rathouský, T. Bein, Chemistry of Materials 21 (2009) 2410.
[22] M. Alvaro, C. Aprile, M. Benitez, E. Carbonell, H. Garcia, Journal of Physical Chemistry B 110 (2006) 661.
[23] K. Shimasaki, N. Suzuki, N. Miyamoto, Y. Yamauchi, Journal of Nanoscience and Nanotechnology 11 (2011) 3256.
[24] M.J. Mosquera, D.M. de los Santos, T. Rivas, Langmuir 26 (2010) 6737.
[25] J.F. Illescas, M.J. Mosquera, Applied Materials & Interfaces 4 (2012) 4259.
[26] J.F. Illescas, M.J. Mosquera, Journal of Physical Chemistry C 115 (2011) 14624.
[27] M.J. Mosquera, A. Montes, D.M. de Los Santos, US Patent US 11/997,356.
[28] M.J. Mosquera, L. Pinho, Spanish Patent No. P201100741. Priority date: June 24, 2011.
[29] M.J. Mosquera, D.M. de los Santos, A. Montes, L. Valdez-Castro, Langmuir 24 (2008) 2772.
[30] E. Beyers, P. Cool, E. Vansant, Journal of Physical Chemistry B 109 (2005) 10081.
[31] A.P. Ferreira Pinto, J. Delgado Rodrigues, Journal of Cultural Heritage 9 (2008) 38.
[32] M. Drdácký, J. Lesák, S. Rescic, Z. Slížková, P. Tiano, J. Valach, Materials and Structures 45 (2012) 505.
[33] UNE-EN 1925, Natural stone test methods, Determination of water absorption coefficient by capillarity, AENOR, 1999.
[34] R.S. Berns, Billmeyer and Saltzman's Principles of Color Technology, Wiley-Interscience, New York, 2000.
[35] ISO 10678, Fine ceramics (advanced ceramics, advanced technical ceramics), Determination of photocatalytic activity of surfaces in an aqueous medium by degradation of methylene blue, ISO, 2010.
[36] P.O. Vasiliev, B. Faure, J.B.S. Ng, L. Bergström, Journal of Colloid and Interface Science 319 (2008) 144.
[37] L. Pinho, F. Elhaddad, D. Facio, M.J. Mosquera, Applied Surface Science (2012), http://dx.doi.org/10.1016/j.apsusc.2012.10.142.
[38] H. Yang, C. Li, H. Gu, T. Fang, Journal of Colloid and Interface Science 236 (2001) 69–103.
[39] P. Mikulasek, R.J. Wakeman, J.Q. Marchant, Chemical Engineering Journal 67 (1997) 97.
[40] X. Zhang, B. Xia, H. Ye, Y. Zhang, B. Xiao, L. Yan, H. Lv, B. Jiang, Journal of Materials Chemistry 22 (2012) 13132.
[41] K. Suttiponparnit, J. Jiang, M. Sahu, S. Suvachittanont, T. Charinpanitkul, P. Biswas, Nanoscale Research Letters 6 (2011) 1.
[42] M. Kosmulski, P. Prochniak, J.B. Rosenholm, Journal of Physical Chemistry C 113 (2009) 12806.
[43] B. Erdem, E.D. Sudol, V.L. Dimonie, M.S. El-Aasser, Journal of Polymer Science Part A: Polymer Chemistry 38 (2000) 4419.
[44] C. Yu, H. Chu, Y. Wan, D. Zhao, Journal of Materials Chemistry 20 (2010) 4705.
[45] H. Shibata, T. Ohkubo, H. Kohno, P. Rangsunvigit, H. Sakai, M. Abe, Journal of Photochemistry and Photobiology A 181 (2006) 357.
[46] M.J. Mosquera, D.M. de los Santos, L. Valdez-Castro, L. Esquivias, Journal of Non-Crystalline Solids 354 (2008) 645.
[47] G. Zhang, J. Yi, J. Shim, J. Lee, W. Choi, Applied Catalysis B 102 (2011) 139.
[48] A. Mirabedini, S.M. Mirabedini, A.A. Babalou, S. Pazokifard, Progress in Organic Coatings 72 (2011) 453.
[49] L. Pinho, M.J. Mosquera, J.C. Hernández-Garrido, J. Calvino, Physical Chemistry Chemical Physics (2012), http://dx.doi.org/10.1039/C2CP42606D.
[50] G. Orcel, L.L. Hench, I. Artaki, J. Jonas, T.W. Zerda, Journal of Non-Crystalline Solids 105 (1988) 223.
[51] G.H. Bogush, C.F. Zukoski, Journal of Colloid and Interface Science 142 (1991) 19.
[52] K. Kosuge, P.S. Singh, Microporous and Mesoporous Materials 44–45 (2001) 139.
[53] A.I. Kontos, I.M. Arabatzis, D.S. Tsoukleris, A.G. Kontos, M.C. Bernard, D.E. Petrakis, P. Falaras, Catalysis Today 101 (2005) 275.
[54] V. Zeleňak, V. Hornebecq, S. Mornet, O. Schäf, P. Llewellyn, Chemistry of Materials 18 (2006) 3184.
[55] M. Kruk, M. Jaroniec, Chemistry of Materials 13 (2001) 3169.
[56] Z. Demjén, B. Pukánsky, E. Foldes, J. Nagy, Journal of Colloid and Interface Science 190 (1997) 427.
[57] M. Sekine, S. Katayama, M. Mitomo, Journal of Non-Crystalline Solids 134 (1991) 199.
[58] A. Prado, C. Airoldi, Journal of Materials Chemistry 12 (2002) 3823.
[59] C.H. Weigel, R. Kellner, Fresenius Zeitschrift fur Analytische Chemie 335 (1989) 663.
[60] X. Gao, I.E. Wachs, Catalysis Today 51 (1999) 233.
[61] P. Innocenzi, Journal of Non-Crystalline Solids 316 (2003) 309.
[62] S.W. Verbruggen, K. Masschaele, E. Moortgat, T.E. Korany, B. Hauchecorne, J.A. Martens, S. Lenaerts, Catalysis Science & Technology 2 (2012) 2311.
[63] F. Babonneau, Polyhedron 13 (1994) 1123.
[64] P.T. Tanev, T. Pinnavaia, Chemistry of Materials 8 (1996) 2068.
[65] G. Wheeler, Alkoxysilanes and the Consolidation of Stone, The Getty Conservation Institute, Los Angeles, CA, 2005.
[66] J. Delgado Rodrigues, A. Ferreira Pinto, D. Costa, Journal of Cultural Heritage 3 (2002) 117.
[67] E. Zendri, G. Biscontin, I. Nardini, S. Riato, Construction and Building Materials 21 (2007) 1098.
[68] C. Miliani, M.L. Velo-Simpson, G.W. Scherer, Journal of Cultural Heritage 8 (2007) 1.
[69] A. Mills, J. Wang, Journal of Photochemistry and Photobiology A: Chemistry 127 (1999) 123.
[70] T.P. Chou, Q. Zhang, B. Russo, G.E. Fryxell, G. Cao, Journal of Physical Chemistry C 111 (2007) 6296.
[71] Z. Zhang, C. Wang, R. Zakaria, J. Ying, Journal of Physical Chemistry B 102 (1998) 10871.
[72] J.T. Carneiro, A.R. Almeida, J.A. Moulijn, G. Mul, Physical Chemistry Chemical Physics 12 (2010) 2744.
[73] Y. Li, Z. Liu, Journal of the American Chemical Society 133 (2011) 15743.
[74] K. Yoshida, M. Makihara, N. Tanaka, S. Ayoagi, E. Nishibori, M. Sakata, E. Boyes, P. Gai, Microscopy and Microanalysis 12 (2011) 264.